An Extended 3D Grain-Based Model for Simulating Nonlinear Deformation and Acoustic Emission Behavior of Weathered Selenite Under Mode I Loading

Rock Mechanics and Rock Engineering
https://doi.org/10.1007/s00603-025-05117-z

ORIGINAL PAPER

An Extended 3D Grain-Based Model for Simulating Nonlinear Deformation and Acoustic Emission Behavior of Weathered Selenite Under Mode I Loading

Xunjian Hu[1,2] · Giuseppe Lacidogna[1,3] · Pedro Marin Montanari[1] · Ediblu Silva Cezar[1] · Jueliang Chen[3] · Angelo Di Tommaso[4]

Received: 5 July 2025 / Accepted: 2 November 2025

Abstract

Understanding the fracture toughness of weathered selenite is critical for assessing the stability of stone cultural heritage under environmental degradation. The three-point bending test is a key method for evaluating the mode I fracture toughness in such brittle materials. This work investigates the influence of weathering degree on the mechanical response, nonlinear deformation behavior, and acoustic emission (AE) characteristics of selenite rock under mode I loading conditions by three-point bending test. A three-dimensional grain-based model (3D-GBM), incorporating 3D Voronoi tessellation and a flat-joint contact model with unbonded contacts, was employed to simulate the heterogeneous crystalline microstructure and pre-existing microcracks typical of weathered selenite. Slightly weathered selenite samples collected from the Garisenda Tower in Bologna were utilized for microparameter calibration. Numerical models representing moderately and highly weathered conditions were developed by systematically increasing microcrack density and width. Numerical results demonstrate that increased weathering intensifies the nonlinear deformation behavior, manifested by more pronounced strain-softening and strain-hardening phases, larger failure displacements, and a marked reduction in mode I fracture toughness from 0.181 to 0.052 MPa·m$^{1/2}$. Force chain analyses reveal a transition toward more heterogeneous stress transmission in highly weathered samples, where load-bearing is concentrated on fewer contacts, thereby promoting dispersed microcrack initiation and coalescence. AE analysis indicates that, with increasing weathering, the spatial distribution of AE events evolves from a localized fracture plane to a more diffuse and random pattern. Concurrently, the maximum AE magnitude decreases, and the *b*-value increases from 2.01 in slightly weathered samples to 3.22 in highly weathered ones, reflecting a shift from brittle to ductile failure mechanisms. A sharp decline in the *b*-value is observed near peak loading, serving as a potential precursor to impending catastrophic failure in weathered selenite. This work underscores the necessity of capturing microstructural heterogeneity and progressive damage processes to better understand weathering-induced degradation in crystalline rocks. The combined application of micromechanical modeling and AE monitoring provides a robust framework for evaluating and preserving stone cultural heritage materials subjected to natural weathering.

Highlights

- A 3D grain-based model coupled with a flat-joint model was developed to simulate weathered selenite with varying weathering degrees.
- Increasing weathering degree leads to lower mode I fracture toughness, more heterogeneous force chain distribution, and a shift from brittle to ductile failure patterns.
- Weathering degree significantly influences the acoustic emission characteristics of selenite, the *b*-value increases from 2.01 in slightly weathered to 3.22 in highly weathered samples.

Keywords Selenite rocks · Weathering degree · 3D grain-based model · Acoustic emission · Flat-joint model · Mode I loading

✉ Giuseppe Lacidogna
giuseppe.lacidogna@polito.it

[1] Department of Structural, Geotechnical and Building Engineering, Politecnico Di Torino, Corso Duca Degli Abruzzi 24, 10129 Turin, Italy

[2] Research Center of Coastal and Urban Geotechnical Engineering, Zhejiang University, Hangzhou 310058, China

[3] College of Architecture and Energy Engineering, Wenzhou University of Technology, Wenzhou 325000, China

[4] Former Professor Alma Mater Studiorum, Università Di Bologna, 40126 Bologna, Italy

Published online: 19 December 2025

1 Introduction

Rock weathering is a complex geological phenomenon driven by the interaction of diverse physical processes (e.g., cyclic wetting and drying, thermal fluctuations) and chemical mechanisms (e.g., oxidation, hydrolysis, dissolution) (Tuğrul 2004; Carroll 2012). These processes are strongly influenced by lithological characteristics and environmental conditions. Due to the widespread occurrence of weathered rocks across the globe and their frequent exposure in civil and geotechnical engineering activities, the mechanical deterioration and microcracking behavior of weathered rocks has attracted substantial research attention (Gupta and Rao 2000; Vivoda Prodan et al. 2017; Monticelli et al. 2020). Such materials are commonly encountered by engineers during site investigations, foundation design, and construction operations. In addition to engineering applications, weathering-induced damage also poses significant threats to the structural stability and preservation of stone cultural heritage. These monuments, which embody outstanding historical, artistic, and scientific value, often suffer progressive degradation after long-term exposure to natural environments. A prominent example is the Garisenda and Asinelli towers (the Two Towers of Bologna) in northern Italy. Constructed primarily from selenite, these structures have undergone extensive weathering due to prolonged environmental exposure and thermal damage caused by internal fires, including the historic use of a forge inside the Garisenda Tower (Dallavalle et al. 2022). Such deterioration has critically compromised the mechanical integrity and long-term stability of the towers. Therefore, a thorough understanding of the mechanical behavior of rocks at different weathering stages is vital for both rock engineering and cultural heritage conservation. In particular, it provides a scientific basis for evaluating structural stability and for designing appropriate support and reinforcement measures.

From a microstructural viewpoint, rocks are generally classified as crystalline or non-crystalline. Crystalline rocks, such as granite and marble, consist of well-defined mineral grains, whereas non-crystalline or clastic rocks, such as sandstone and shale, comprise loosely cemented particles with poorly developed crystalline textures. As a typical non-crystalline rock, sandstone has been widely employed in stone heritage structures such as the Palazzo Ducale in central Italy (Mammoliti et al. 2024), the Angkor temples in Cambodia (Waragai 2016), the Dazu Grottoes (Lin et al. 2024; Liu et al. 2025), and the Leshan Giant Buddha in southwestern China (Sun et al. 2025a). Rock weathering significantly influences both the macroscopic mechanical response and microcrack propagation in sandstone. For example, the sandstone of the Leshan Giant Buddha is primarily affected by chemical weathering, which degrades and removes cementing agents from its surface (Sun et al. 2025a). The extent of weathering is largely controlled by the rock textural attributes, especially its pore size and distribution (Labus and Bochen 2012; Sun et al. 2025a). Sandstones characterized by large and densely distributed pores facilitate water infiltration, leading to enhanced colloid leaching and progressive pore enlargement. These microstructural alterations ultimately weaken the rock, reducing both its static and dynamic strength (Zhao et al. 2017; Ke et al. 2018). The failure mode, characteristic stresses, and appropriate conservation measures for such heritage materials are intrinsically linked to the microstructural properties of sandstone, including grain size and cementation (Liu et al. 2025).

In addition to non-crystalline rocks, crystalline rocks such as granite and marble have been widely used in historic stone structures due to their durability and aesthetic appeal. For example, granite was used in the construction of the Our Lady of the Assumption Church in Valdemorillo and the Valdemaqueda Bridge in the Madrid region of Spain (Fort et al. 2013), while marble was extensively applied in the Forbidden City and the Temple of Heaven in the Beijing region of China (Liu et al. 2019). Crystalline rocks differ markedly from sandstones in petrographic properties, exhibiting low porosity and a compact microstructure. Their internal heterogeneity arises from mineral grain aggregation, cleavage planes, and inherent microcracks. Macroscopic mechanical behaviors, such as deformation, strength, and crack development, are strongly influenced by grain-scale features such as grain boundary heterogeneity (Hu et al. 2024a) and mineral grain size distribution (Li et al. 2020; Huang et al. 2021; Hu et al. 2024b). The degree of weathering exerts a significant impact on these properties. For example, the uniaxial compressive and tensile strengths of granite decrease markedly with increasing weathering intensity (Ye et al. 2025). Jaques et al. (2020) reported a reduction of up to 99% in uniaxial compressive strength in highly weathered granitic rock, which they attributed to pronounced differences in internal structure across weathering stages. Strongly weathered granite displays a flocculent internal texture with visible exterior cracks; moderately weathered granite shows interlaced pore structures and minor surface cracks; while slightly weathered granite retains an intact crystalline structure with distinct mineral luster and minimal external damage (Ye et al. 2025). Given the inherently low tensile strength of rock, fracture toughness under mode I loading is a critical parameter in assessing the stability of weathered rocks and preserving stone heritage (Wang et al. 2024a). Selenite, composed primarily of large, twinned gypsum crystals, is representative of crystalline rock and was widely used in historical architecture of the Bologna region due to its visual appeal and workability (Dallavalle et al. 2022). Studies have shown that the fracture toughness of crystalline rocks

degrades significantly under weathering processes such as freeze–thaw cycles (Dehghani and Faramarzi 2019; Niu et al. 2024) or high-temperature treatment (Hu et al. 2023a, 2023b). However, the micromechanical mechanisms linking weathering and fracture toughness in rocks like selenite remain poorly understood.

Recently, numerical modeling techniques have emerged as powerful tools to investigate grain-scale effects on the mechanical behavior of crystalline rocks (Lan et al. 2010). Grain-based models (GBMs), such as PFC2D-GBM (Potyondy 2010; Hu et al. 2020, 2022; Zhang et al. 2024) and UDEC-GBM, use polygonal grains constructed via Voronoi tessellation to explicitly represent mineral assemblies. These models enable the simulation of macro-mechanical behavior as an emergent outcome of grain-scale interactions. However, conventional 2D models are limited in their ability to accurately capture the three-dimensional geometry and failure mechanisms of rocks like selenite. Assumptions of plane stress or plane strain in 2D simulations constrain their effectiveness in representing 3D fracture propagation and coalescence (Li et al. 2020; Zhou et al. 2025). To address these limitations, more advanced three-dimensional GBMs (3D-GBMs) are necessary. Several 3D-GBMs have been developed for simulating mechanical behavior and microcracking under both static (Ghazvinian et al. 2014; Li et al. 2020; Yahaghi et al. 2023; Bu et al. 2025; Zhou et al. 2025) and dynamic loading conditions (Yu et al. 2022; Gong et al. 2025). The microstructural heterogeneity of crystalline rocks significantly influences their mechanical response (Lan et al. 2010; Mahabadi et al. 2014; Huang et al. 2021; Hu et al. 2024a; Rasmussen and Min 2024), including properties such as fracture toughness, elastic modulus, and strength, which are governed by microparameters in GBMs. It is possible to have non-linear models using linear elastic contacts when heterogeneity is represented, for example, by means of stiffness and strength properties that follow some statistical distribution. An example of work that achieves realistic nonlinear behavior using such an approach for a complex anisotropic rock was presented by Rasmussen and Min (2024). However, most existing GBMs rely on linear elastic contact models, making them suitable only for fresh rocks with near-linear pre-peak behavior. These models fail to capture the nonlinear stress–strain response observed in highly weathered crystalline rocks (Gupta and Rao 2000; Sarfarazi et al. 2024). In the Garisenda Tower, centuries of exposure to environmental agents such as rainfall and fire have induced a wide range of weathering stages in the selenite blocks, resulting in highly complex mechanical behavior. Given its unique crystalline nature and widespread use in Italian heritage structures, a better understanding of the mechanical and microcracking behavior of selenite is essential for its conservation. Conventional GBMs fall short in this regard. Therefore, one of the aims of this work is to develop an extended 3D-GBM capable of reproducing the microstructural features of selenite across different weathering stages.

Nondestructive structural health monitoring (SHM) plays a vital role in the diagnosis and preservation of stone heritage buildings (Lacidogna et al. 2015). SHM systems can be classified based on measurement duration, frequency, target parameters, and monitoring techniques (Baraccani et al. 2021; Pesci et al. 2024). Acoustic emission (AE) is a widely used nondestructive technique for real-time monitoring. It captures transient elastic waves generated by microstructural changes such as crack initiation and propagation. AE technology has been applied to various heritage sites, including the Garisenda Tower (Marin Montanari et al. 2024). In its basement, selenite blocks exhibit a wide range of weathering intensities, ranging from slight to moderate, while highly weathered selenite is found in areas affected by historical fires. In these regions, the microcrystalline structure is severely pulverized, compromising mechanical integrity (Dallavalle et al. 2022). AE responses during failure vary significantly with the degree of weathering. Studies on sandstone, marble, and granite have shown that rocks subjected to freeze–thaw cycles display distinct AE patterns compared to fresh specimens (Ullah et al. 2023; Zhou et al. 2023). Treated rocks exhibit higher and more stable AE energy accumulation. Similarly, heating–cooling cycles result in smoother AE energy curves and increasing *b*-values due to the progressive development of microcracks (Ge and Sun 2018). To assess the stability of monuments such as the Garisenda Tower, AE-based zonal evaluations offer a promising approach. However, studies on AE behavior in weathered crystalline rocks, particularly selenite, remain scarce.

The primary objective of this work is to propose an extended 3D-GBM for investigating the mechanical response, nonlinear deformation, and AE characteristics of selenite subjected to varying degrees of weathering under mode I loading. Initially, three-point bending tests were conducted on slightly weathered selenite samples collected from the Garisenda Tower of Bologna. These experiments were then replicated using a 3D-GBM incorporating a flat-joint contact model, implemented in PFC3D 5.0 (Itasca Consulting Group Inc. 2014). Finally, by constructing numerical models of selenite at different weathering levels, the nonlinear deformation behavior and corresponding AE responses under mode I loading were systematically analyzed.

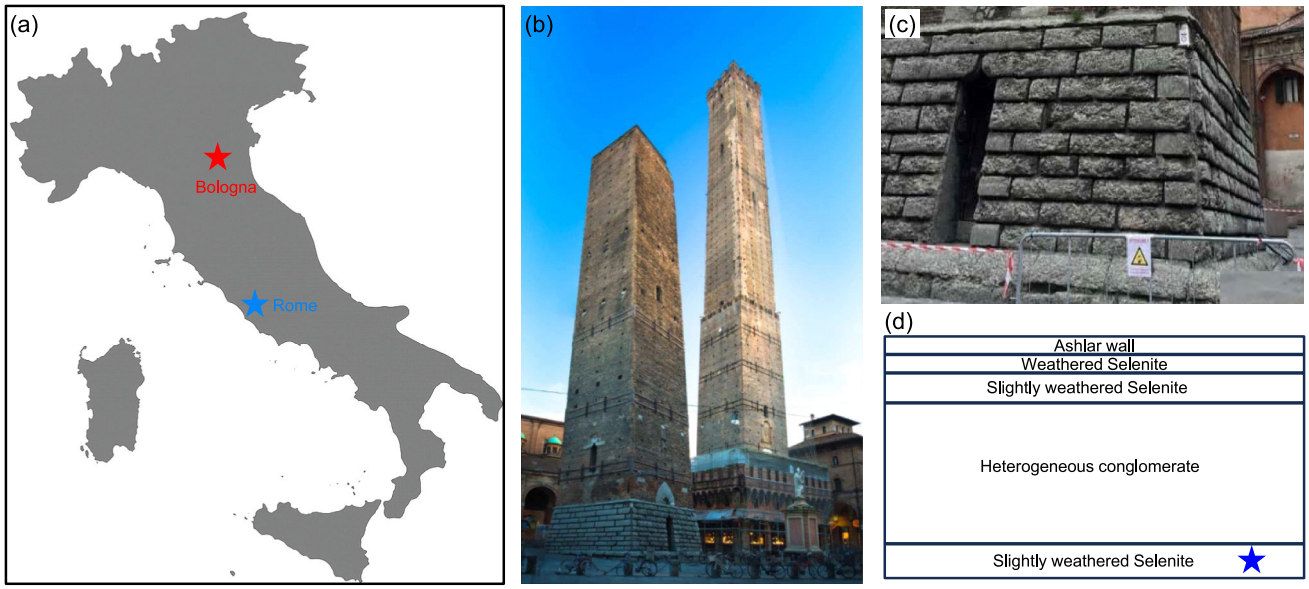

Fig. 1 Sampling location and structural details of the Garisenda Tower. **a** Map of Italy showing the sampling location in Bologna; **b** Image of Garisenda (left) and Asinelli Tower (right) (Pesci et al. 2024); **c** Close-up view of the base of Garisenda Tower; **d** Schematic cross-section of the tower structure. Note: the blue pentagram in (**d**) indicating the location of slightly weathered selenite sampling

2 Materials and Methods

2.1 Selenite Sample

The City of Bologna, located in northern Italy (Fig. 1a), is renowned for its rich cultural heritage. Among its most iconic landmarks are the Garisenda and Asinelli towers, widely recognized as enduring symbols of the city (Fig. 1b). Together with numerous civic towers and tower houses constructed during the Middle Ages, these monuments represent a significant component of Italian architectural heritage, particularly in the northern and central regions of the country. The Garisenda Tower, originally completed in the early twelfth century, once stood at a height of 60 m, but was reduced by approximately 12 m during the mid-fourteenth century. Its base is faced with selenite stone, added in the late nineteenth century (Fig. 1c). The tower rests on a geologically complex foundation composed of highly variable subsoil strata with limited lateral continuity, which has led to uneven settlement and is regarded as a primary cause of the current inclination. Historical records and recent investigations suggest that earlier construction activities in the surrounding area likely introduced additional disturbances to the load distribution and subsoil stress regime, further contributing to differential settlement (Bertolini et al. 2023). These findings emphasize the necessity of continuous AE monitoring to ensure the structural integrity and long-term stability of the Garisenda Tower. The wall stratigraphy of the Garisenda Tower, progressing from the exterior to the interior, includes an outer ashlar masonry layer, followed by weathered selenite, slightly weathered selenite, a heterogeneous conglomerate, and another layer of slightly weathered selenite (Fig. 1d).

In this work, rock samples were obtained by coring from the innermost layer of the tower structure (Fig. 1d). The sampling was conducted in the basement area of the Garisenda Tower, using a borehole with an approximate diameter of 75 mm. Representative selenite samples were selected for subsequent three-point bending tests to investigate their mechanical properties and deformation behavior. Uniaxial compression tests were conducted on six cylindrical samples with varying slenderness ratios. The results indicate that the slightly weathered selenite samples exhibit average uniaxial compressive strength and elastic modulus values of 10.23 MPa and 987.50 MPa, respectively, with a measured Poisson's ratio of 0.18. Selenite primarily consists of gypsum ($CaSO_4{\cdot}2H_2O$), forming the dominant mineral phase, as verified by X-ray diffraction (XRD) analysis. The grain boundaries are typically filled with a clay-rich matrix or other fine-grained argillaceous cementing materials. With increased weathering, the selenite undergoes a range of microstructural modifications, including the development of microcracks and micropores, volumetric instability, dehydration of gypsum, and subsequent formation of a newly interlocked microcrystalline gypsum framework. These changes contribute to the progressive degradation of the original rock fabric (Dallavalle et al. 2022).

2.2 3D Grain-Based Model

Potyondy (2010) introduced a GBM approach capable of representing the realistic microstructure of crystalline rocks. In this framework, distinct micromechanical parameters are assigned to two types of contacts: intragrain contacts (IG contacts), which occur within mineral grains, and grain boundary contacts (GB contacts), which lie along grain boundaries. This differentiation allows for the simulation of heterogeneous mechanical responses characteristic of natural rock materials. In the original GBM formulation, IG contacts were modeled using the linear parallel bond model, while GB contacts were represented by the smooth-joint model (Potyondy 2010). Building on this foundation, various combinations of contact models have since been proposed. For example, the flat-joint model has been used for IG contacts in combination with the smooth-joint model for GB contacts (Wang et al. 2021; Zhao et al. 2021), while some studies have applied the linear parallel bond model to both contact types (Hu et al. 2023c). Although these approaches have successfully replicated the microstructural features and mechanical responses of intact crystalline rocks, they have been primarily limited to fresh specimens, which typically exhibit a nearly linear-elastic stress–strain response during the pre-peak stage (Saadat et al. 2021; Wang et al. 2021, 2025; Zhao et al. 2021; Hu et al. 2023c; Zhang et al. 2024; Zhou et al. 2025).

In contrast, weathered rocks commonly contain a high density of microcracks, and their mechanical response is characterized by pronounced nonlinear behavior associated with crack closure during initial loading (Gupta and Rao 2000; Huang et al. 2021; Sarfarazi et al. 2024; Ye et al. 2025). Several methods have been proposed to capture this nonlinear behavior. One approach involves using a variable-stiffness joint contact model (Mehranpour and Kulatilake 2017), while another involves setting initial gaps in the linear parallel bond model (Ji et al. 2018). The latter technique, implemented in PFC2D, enables the generation of a large number of microcracks without significantly increasing computational costs. However, this approach reduces the degree of particle interlocking, making it difficult to simulate a progressive reduction in tangent modulus during uniaxial compression (Ji et al. 2018). The flat-joint model, originally proposed by Potyondy (2012), offers rotational constraint due to grain interlocking through a polygonal grain representation, which is simpler than clusters of discrete particles. Additionally, flat-joint contacts, which are surface-based rather than point-based, more accurately represent the propagation of stress waves and are thus better suited for simulating AE behavior (Peng et al. 2024). The flat-joint model in PFC, along with Voronoi-based grain approaches, has been widely used to investigate key aspects such as fracture initiation (Zhou et al. 2019), size effects (Li et al. 2018a), and AE behavior (Ma et al. 2021) of rock materials. To accurately reproduce both the microstructural features and the nonlinear mechanical response of weathered crystalline rocks such as selenite, this work proposes an extended 3D-GBM, wherein both IG and GB contacts are implemented using the flat-joint model.

As shown in Fig. 2a, flat-joint contacts maintain a face-to-face configuration between particles, regardless of whether the bonds are intact or broken (Itasca Consulting Group Inc. 2014). This feature makes the flat-joint model particularly effective in simulating narrow microcracks and enables the reproduction of nonlinear crack closure behavior in weathered selenite. By explicitly differentiating IG and GB contacts, the GBM can simulate fracture development in both regions, allowing the identification of four distinct microcrack types during loading: intragrain tensile (IGT) cracks, intragrain shear (IGS) cracks, grain boundary tensile (GBT) cracks, and grain boundary shear (GBS) cracks (Fig. 2b).

The contact interface of the flat-joint model is discretized into multiple sub-elements (Fig. 2a), each of which may be either bonded or unbonded. Damage is accumulated through the progressive breakage of bonded sub-elements. The mechanical behavior of the flat-joint model is illustrated in Fig. 2c and d (Itasca Consulting Group Inc. 2014). Bonded sub-elements behave in a linear-elastic manner until their strength threshold is exceeded, after which they transition to an unbonded state (Fig. 2c). Unbonded elements also behave elastically but incorporate frictional sliding governed by the Coulomb failure criterion (Fig. 2d). A comprehensive description of the flat-joint model is available in the PFC user manual (Itasca Consulting Group Inc. 2014).

Conventional flat-joint models for intact rock often face challenges in reproducing the nonlinear crack-closure stage observed during loading (Wang et al. 2021; Zhao et al. 2021). These difficulties arise because the standard configurations assume that most contacts are either fully or partially bonded, without initial gaps. Introducing unbonded contacts with predefined gaps provides a way to represent initial microcracks and capture the macroscopic nonlinear deformation behavior of weathered rocks. In the flat-joint framework, each microcrack is represented by an unbonded contact. For weathered samples, two key microstructural parameters are used to characterize the crack network: crack width and crack density. Crack width refers to the initial gap between the flat-joint surfaces (Fig. 2a), while crack length is defined by the diameter of the smaller of the two particles forming the contact. Crack density is quantified as the ratio of unbonded contacts to the total number of contacts. Numerous studies have performed sensitivity analyses on these microparameters. Crack density predominantly influences the extent of the crack-closure stage, whereas crack width affects the evolution of the tangent modulus. As crack density increases, the stress–strain response exhibits a more

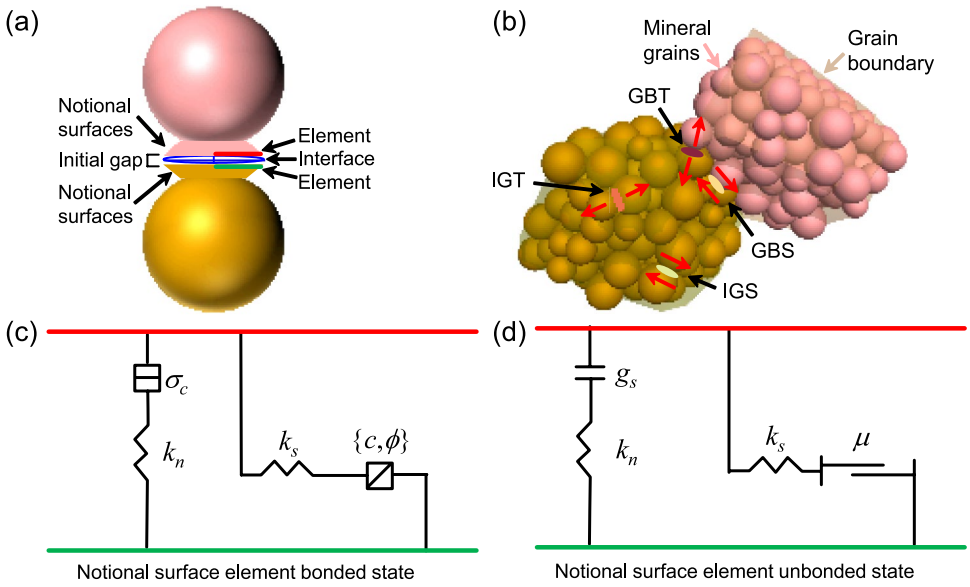

Fig. 2 Basic principle of 3D GBM (modified after Itasca Consulting Group Inc (2014)). **a** Flat-joint model; **b** Schematic diagrams of four types of Microcracks in 3D GBM; **c** Notional surface element bonded state; **d** Notional surface element unbonded state. Microcrack types in (**b**) are abbreviated as follows: intragranular tension (IGT) crack, intragranular shear (IGS) crack, grain boundary tension (GBT) crack and grain boundary shear (GBS) crack. Note: σ_c tensile strength, k_n normal stiffness, k_s shear stiffness, c cohesion, ϕ friction angle, g_s surface gap, and μ friction coefficient

pronounced nonlinear closure region and a gradual transition from brittle to ductile behavior (Ye et al. 2022; Peng et al. 2024).

2.3 Modeling of the Semi-circular Bend Selenite Sample

The slightly weathered selenite (SWS) samples examined in this work were collected from the Garisenda Tower in Bologna, Italy. The semi-circular bend (SCB) specimen is a widely accepted configuration for determining the mode I fracture toughness of rock materials, owing to its simple specimen preparation procedure. It is also recommended by the International Society for Rock Mechanics (ISRM) (Kuruppu et al. 2014). According to ISRM guidelines, the ratio of notch length to specimen radius should lie between 0.4 and 0.6. However, due to the fragile nature of the weathered selenite samples obtained in this work, specimen preparation was challenging. In particular, the manual cutting of notches was highly constrained, limiting the achievable notch length to only 3 mm, which deviated from the recommended ratio. For SCB specimen preparation, selenite cores with a radius of 37.5 mm and a thickness of 20 mm were halved along the diameter to produce two semi-circular discs. A straight notch, 3 mm in length and 1 mm in width, was introduced perpendicular to the flat surface, originating from the center of the disc. The specific geometrical parameters of the SCB specimen are illustrated in Fig. 3a. A photograph of the prepared selenite SCB sample is shown in Fig. 3b. This specimen was subsequently subjected to three-point bending tests under mode I loading conditions, accompanied by real-time AE monitoring to evaluate both its mechanical properties and AE characteristics.

Voronoi tessellation has been widely employed to simulate the microstructure of crystalline rocks such as granite (Yu et al. 2022; Hu et al. 2023c), marble (Li and Bahrani 2021), and salt rock (Li et al. 2020). It is recognized as one of the most effective and appropriate techniques for constructing polygonal polycrystalline models, such as the 3D-GBM utilized in this work. The three-dimensional Voronoi tessellation was applied to replicate the mineral grain distribution of SWS, enabling a realistic representation of its internal microstructure. A 3D Voronoi tessellation is a partition of a domain of 3D space, $D \in \mathbb{R}^3$, into a collection of cells. Given a number of seed points in D, $\{S_i(x_i)\}$ for $i = \{1, \ldots, N\}$, every seed is assigned a Voronoi cell, C_i, as follows:

$$Ci = \left\{ P(x) \in D \middle| d(P, S_i) \le d(P, S_j), \forall j \ne i \right\} \quad (1)$$

where $d(.,.)$ is the Euclidean distance. The seed locations are randomly chosen from a uniform distribution in the domain. In this study, 3D Voronoi tessellations were generated using Rhinoceros software within a spatial domain that matched the geometry of the selenite SCB specimens tested in the laboratory (Fig. 3c). The generated Voronoi tessellation was subsequently imported into PFC3D in STL file format. The numerical model was constructed using clusters of spherical particles (balls), with ball radii uniformly distributed between 0.50 and 0.83 mm. By integrating the ungrouped particle assembly with the Voronoi structure, particles located within each Voronoi cell were grouped to represent individual gypsum grains (Fig. 3d). Each mineral grain was therefore modeled as a cluster composed of numerous smaller balls. The modeled SWS sample comprised 28,112 balls and 163,166 contacts, organized within 238 Voronoi

cells. On average, each cell contained approximately 118 balls and 685 contacts, which is sufficient to represent the internal mechanical behavior of gypsum grains (Li et al. 2018b, 2020; Hu et al. 2024a). The interface between two adjacent mineral grains was defined as a grain boundary (Fig. 3e), and contacts along these boundaries were assigned distinct micromechanical parameters from those within the mineral grains (Fig. 3f), in order to account for the mechanical heterogeneity between intragrain and intergrain regions. The grain size and sphericity of the 3D Voronoi tessellations used to simulate selenite (Fig. 3g and h) reflect the geometric heterogeneity inherent in the modeled microstructure. The average grain size was approximately 0.35 cm, classifying the modeled selenite as coarse-grained according to established criteria (Caselle et al. 2019a, b).

It is important to acknowledge that current numerical approaches for simulating the grain-scale micromechanics of selenite possess inherent limitations in fully reproducing its complex geometric heterogeneity. A certain level of simplification is both necessary and acceptable (Lan et al. 2010; Hu et al. 2023c; Zhou et al. 2025). In line with this, the modelled SWS sample developed in this work does not attempt to replicate the exact geometry of mineral grains or to capture all weathering-induced features, such as micropores, microcracks, or mineral phase transitions in full detail. Rather, the modeling focuses on two primary factors that play a dominant role in influencing the mechanical behavior of weathered crystalline rocks: the overall microstructural configuration, represented by 3D Voronoi tessellations, and the inclusion of microcracks, incorporated through the flat-joint model.

This work aims to investigate the influence of weathering degree on the mode I fracture toughness of selenite. Under static loading conditions, SCB specimens were subjected to symmetric three-point bending with a span length of 50 mm until failure occurred (Fig. 3a). The mode I fracture toughness (K_{IC}) for both experimental and numerical specimens was determined based on the measured peak load (P_{max}) and the geometrical parameters of the SCB samples, as defined by Kuruppu et al. (2014):

$$K_{IC} = Y' \frac{P_{max}\sqrt{\pi a}}{2RB} \tag{2}$$

where a is the notch length, R is the radius of samples, B is the thickness of samples. The stress intensity factor Y' is a dimensionless parameter that depend on the sample geometry and loading conditions. According to the results reported by Lim et al. (1993), the values of Y' used in this work is approximately 3.8210.

Three-point bending tests were conducted using a servo-hydraulic Materials Test System (MTS) at the Department of Structural, Geotechnical and Building Engineering, Politecnico di Torino. The SCB specimens were subjected to monotonic three-point bending at a constant loading rate of 0.02 mm/min until rock failure. The experimental setup comprised a loading frame with integrated force and displacement measurement systems, a data acquisition computer, and two support rollers on which the SCB specimen was positioned. Additionally, an AE monitoring system was employed to capture real-time signals during the loading process. Each test was terminated when a pronounced drop in axial load was observed, indicating the onset of specimen failure.

2.4 Modelling Acoustic Emission by Moment Tensor Calculation

When a flat-joint contact fails, the bonded particles separate, inducing deformation in the surrounding contacts (Hazzard and Young 2000). This local redistribution of stress leads to variations in contact forces around the failure zone. In the 3D-GBM, microcracks that occur in close spatial and temporal proximity are grouped as a single AE event. The duration of each AE event is estimated based on the assumption that crack propagation occurs at half the shear wave velocity of the modeled selenite. Consequently, if a subsequent microcrack forms within the influence zone of an ongoing crack, it is considered part of the same AE event, and the source area is updated to include all associated source particles. This approach allows the formation of AE events composed of multiple microcracks, resulting in more realistic distributions of AE magnitudes. The following is the formula for calculating the AE moment tensor **M** (Hazzard and Young 2004):

$$M_{ij} = \sum \Delta F_i R_j \tag{3}$$

where ΔF_i is the ith component of change in flat-joint contact force, and R_j corresponds to the jth component of the distance between the contact force and the microcrack center. The scalar moment M_0 is determined as follows:

$$M_0 = \sqrt{\frac{\sum_{j=1}^{3} m_j^2}{2}} \tag{4}$$

where m_j is the jth eigenvalue of moment tensor **M**. The maximum value of the scalar moment M_0 is used to compute the magnitude M associated with an AE event:

$$M = \frac{2}{3}\log M_0 - 6 \tag{5}$$

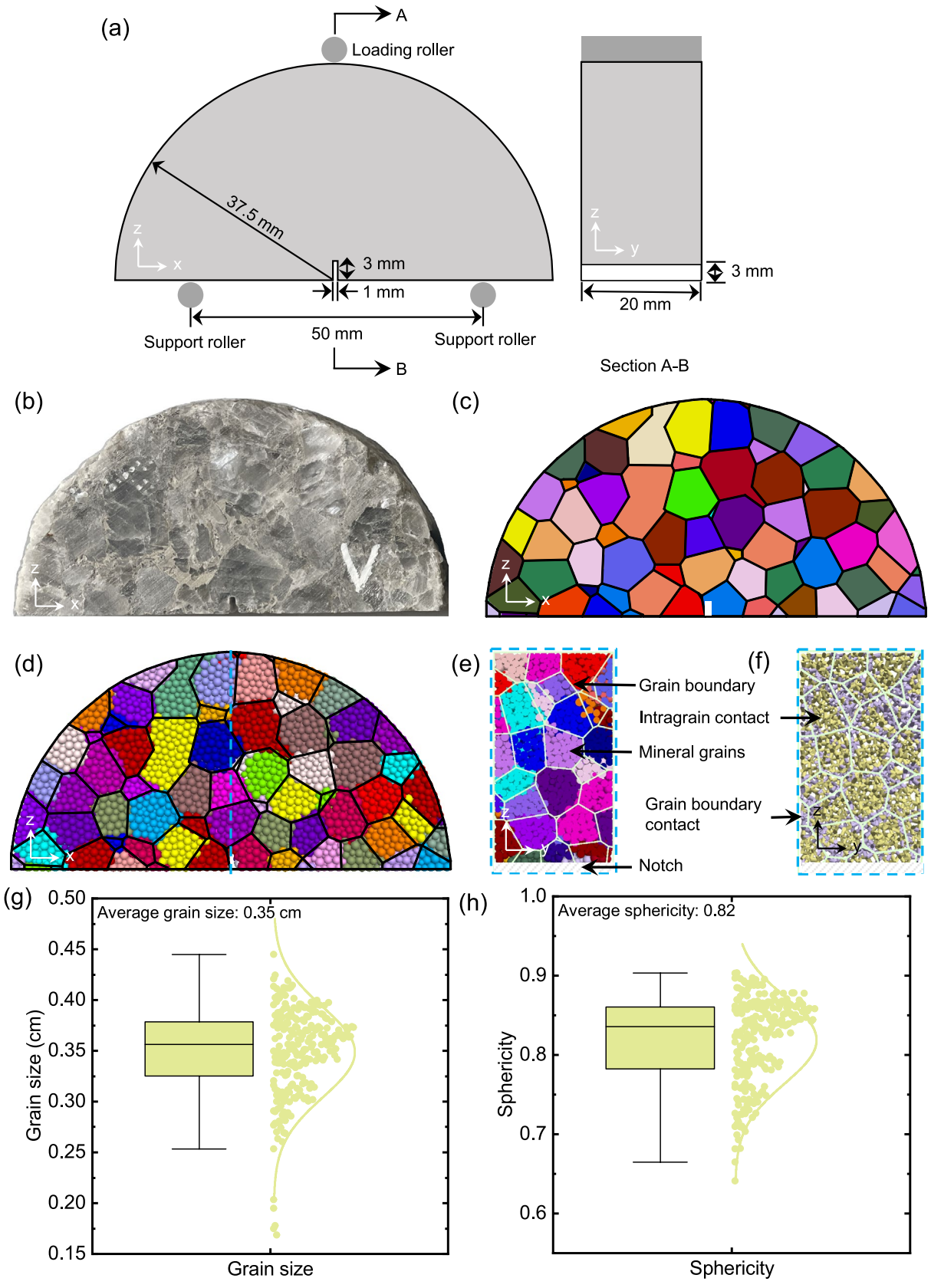
(a)
A
Loading roller
37.5 mm
3 mm
1 mm
50 mm
Support roller
Support roller
B
3 mm
20 mm
Section A-B
(b)
(c)
(d)
(e)
(f)
Grain boundary
Intragrain contact
Mineral grains
Grain boundary contact
Notch
(g)
Average grain size: 0.35 cm
Grain size (cm)
Grain size
(h)
Average sphericity: 0.82
Sphericity
Sphericity

◂**Fig. 3** The modeling process of SCB selenite sample by 3D GBM. **a** Geometry of SCB sample; **b** SCB selenite sample collected from the Garisenda Tower in Bologna; **c** 3D Voronoi tessellations representing the microstructure of selenite; **d** Grouped 3D GBM for selenite; **e** Cross-sectional view of the SCB selenite model; **f** Illustration of intragrain contacts and grain boundary contacts; **g** Grain size distribution diagram consisting of a box plot (left) and a scatter plot (right); **h** Sphericity distribution diagram consisting of a box plot (left) and a scatter plot (right). Note: in (**c**), (**d**), and (**e**), different colors represent individual gypsum mineral grains

The moment tensor can be divided into isotropic and deviatoric parts:

$$\mathbf{M} = \frac{tr(\mathbf{M})}{3}\begin{bmatrix} 1 & 0 & 0 \\ 0 & 1 & 0 \\ 0 & 0 & 1 \end{bmatrix} + \begin{bmatrix} m_1^* & 0 & 0 \\ 0 & m_2^* & 0 \\ 0 & 0 & m_3^* \end{bmatrix} \tag{6}$$

where $tr(\mathbf{M})$ is the sum of eigenvalues, and m_i^* is the deviatoric eigenvalues ($i = 1, 2, 3$). Depending on their isotropic/deviatoric ratio λ, the AE event is classified as "tensile," "shear," or "implosive" type. The isotropic/deviatoric ratio is given by (Feignier and Young 1992):

$$\lambda = \frac{tr(\mathrm{M}) \times 100\%}{\left| tr(\mathrm{M}) + \sum m_i^* \right|} \tag{7}$$

An AE event can be characterized as "tensile" ($\lambda > 30\%$), "shear" ($-30\% \le \lambda \le 30\%$), or "implosive" ($\lambda < -30\%$) (Feignier and Young 1992). An additional technique for analyzing the moment tensor $\mathbf{M}$ involves its decomposition into three fundamental components: isotropic (ISO), double couple (DC), and compensated linear vector dipole (CLVD) (Hudson et al. 1989; Vavryčuk 2015). To facilitate the interpretation of failure mechanisms, two scalar parameters T (representing the deviatoric component) and k (representing the isotropic component) were derived from the moment tensor of each AE event. T is a measure of the deviatoric component of the source ranging from a pure positive CLVD at -1 to a pure negative CLVD at $+1$ and passing through a pure double couple at the origin. k is a measure of the isotropic component of the source and varies from a pure explosion at $+1$ to a pure implosion at -1. These values are calculated by (Hudson et al. 1989; Vavryčuk 2015):

$$T = \frac{2m_2^*}{\max\left(\left|m_1^*\right|, \left|m_3^*\right|\right)} \tag{8}$$

$$k = \frac{\frac{1}{3}tr(\mathbf{M})}{\left|\frac{1}{3}tr(\mathbf{M})\right| + \max\left(\left|m_1^*\right|, \left|m_3^*\right|\right)} \tag{9}$$

2.5 Microparameters Calibration

The investigated selenite in this work is a monomineralic crystalline rock predominantly composed of gypsum grains and their associated grain boundaries. Despite its mineralogical uniformity, previous micro-scale investigations have demonstrated that the mechanical properties of gypsum exhibit notable heterogeneity at the grain scale, primarily due to differences in microstructural features (Caselle et al. 2019a, b; Ramon et al. 2021). For example, the strength and stiffness of gypsum vary significantly along different crystallographic cleavage planes (Mukherjee and Misra 2024). To balance computational efficiency with model fidelity, the intrinsic microparameters of all gypsum grains were assumed to be identical. However, heterogeneity is still preserved in the modeled samples due to the random distribution of unbonded contacts introduced by the flat-joint contact model and the inherent variability in the 3D structure of the Voronoi cells. A similar approach was adopted for defining the microparameters associated with grain boundaries.

In the 3D-GBM, calibration of microparameters is a critical step to ensure that the numerical model reproduces the experimentally observed macroscopic responses, including peak load, mode I fracture toughness, and generalized stiffness (defined as the slope of the load–displacement curve). The SWS specimens obtained from the Garisenda Tower in Bologna served as reference samples for calibrating the microparameters of the 3D-GBM. Most microparameters reflect the intrinsic properties at the grain scale and are not readily measurable through conventional laboratory testing, particularly when both intragrain and grain boundary contacts are explicitly modeled, which significantly increases the heterogeneity of the model. Therefore, a trial-and-error approach, widely used in GBMs (Potyondy 2010), was adopted to iteratively determine suitable microparameter values. The calibrated microparameters for modeled selenite SCB samples with varying degrees of weathering are summarized in Table 1.

A qualitative and quantitative comparison between the numerical simulations and experimental observations demonstrated similar failure patterns and mechanical responses (Fig. 4). Figure 4a and b show the experimental SCB samples before and after loading, respectively, while Fig. 4c and d depict the corresponding numerical results at the same stages. At the macroscopic scale, a tensile macrocrack initiated at the notch tip and propagated toward the loading point, consistent with the tensile stress concentration induced by the three-point bending configuration applied to the SCB specimens. Owing to the pronounced heterogeneity of the SWS samples including both geometric and mechanical inhomogeneity the macroscopic fracture surfaces exhibited

Table 1 Calibrated microparameters for modelled selenite SCB samples

Microparameter	SWS	MWS	HWS
Basic parameters			
Minimum radius of particle (mm)	0.50	0.50	0.50
Particle radius ratio	1.66	1.66	1.66
Particle density (kg/m^3)	2400	2000	1600
Effective modulus (GPa)	1.42	1.42	1.42
Crack width (1×10^{-5} m)	0.9	1.5	2.0
Crack density	0.54	0.67	0.71
Mineral grain (Flat-joint model)			
Modulus (GPa)	1.42		
Radius multiplier	1.0		
Normal-to-shear stiffness ratio	1.0		
Tensile strength (MPa)	9.2		
Cohesion (MPa)	15.3		
Friction angle (°)	20		
Grain boundary (Flat-joint model)			
Modulus (GPa)	1.25		
Radius multiplier	1.0		
Normal-to-shear stiffness ratio	1.0		
Tensile strength (MPa)	6.5		
Cohesion (MPa)	10.2		
Friction angle (°)	15		

significant irregularity and angular deviation. From a grain-scale perspective, both experimental and numerical fracture surfaces were composed of IG and GB cracks. The coalescence and propagation of these cracks contributed to the formation of a complex three-dimensional fracture path. Previous studies have emphasized the role of weak planes, such as grain boundaries, in influencing crack initiation and deflection near the notch tip (Wong et al. 2019). In weathered selenite, this effect is further amplified by the well-developed cleavage planes of gypsum. Thus, both cleavage planes and grain boundaries significantly influence the crack propagation process. Figure 4e compares the load–displacement curves obtained from numerical modeling and laboratory testing of SCB samples under mode I loading. The numerical results exhibit good agreement with the experimental data, particularly in capturing the initial nonlinear crack-closure stage. This behavior is accurately reproduced by the extended 3D-GBM developed in this work, which incorporates the flat-joint model and accounts for pre-existing microcracks. The modeled load–displacement response matches well with the observed experimental curve, validating the effectiveness of the numerical approach. The simulated mechanical properties also align well with experimental measurements. The mode I fracture toughness derived from numerical simulation is 0.181 MPa·m$^{1/2}$, while the corresponding laboratory value is 0.185 MPa·m$^{1/2}$, resulting in a relative error of only 2.16%. Similarly, the generalized stiffness obtained from numerical modeling is 2.061 kN/mm, compared to 2.280 kN/mm from laboratory testing, demonstrating satisfactory agreement. These results confirm the capability of the 3D-GBM to reliably replicate the mechanical behavior of weathered selenite.

In terms of AE characteristics, AE events initiated at approximately 25% of the peak load during the early loading stage in both simulations and experiments (Fig. 4e). As the load increased, the number of AE events steadily rose. The temporal evolution of numerically simulated AE activity closely mirrored experimental observations, supporting the validity of using moment tensor theory to simulate AE behavior within the 3D-GBM framework. Nevertheless, the total number of AE events recorded in numerical simulations was significantly higher than in experiments. This discrepancy is attributed to the idealized conditions in numerical modeling, where all acoustic emission events are recorded regardless of their magnitude. In contrast, experimental AE recordings are subject to limitations such as sensor placement and quantity, amplitude thresholds, and other practical constraints, leading to under-recording of low-amplitude events.

The above analysis demonstrates that the microparameters of SWS listed in Table 1 effectively reproduce the mechanical properties, microcrack behavior, and AE characteristics observed in the experimental selenite samples. To simulate selenite with varying degrees of weathering, this work focuses on a key feature of the weathering process: the increase in microcracks. This phenomenon has been consistently confirmed by numerous experimental studies across different weathering stages (Luque et al. 2011; Carroll 2012; Eppes and Keanini 2017; Okewale and Grobler 2021; Ye et al. 2025). Other aspects of rock weathering, such as changes in microporosity, volumetric variations, and phase transitions, are not addressed in the present work (Carroll 2012; Yang et al. 2025). Starting from the microparameters calibrated for the modeled SWS samples (Fig. 5a), crack width and crack density were systematically increased to develop two additional heterogeneous 3D-GBMs representing moderately weathered selenite (MWS, Fig. 5b) and highly weathered selenite (HWS, Fig. 5c). The corresponding microparameters for MWS and HWS are summarized in Table 1. Specifically, the crack width and crack density for MWS are 1.5×10^{-5} m and 0.67, respectively, while those for HWS are 2.0×10^{-5} m and 0.71, respectively. It is important to note that the MWS and HWS models were not derived from in-situ core samples taken from the Garisenda Tower in Bologna, due to practical limitations and concerns about potentially compromising the tower's structural stability. Thus, these modeled MWS and HWS samples should

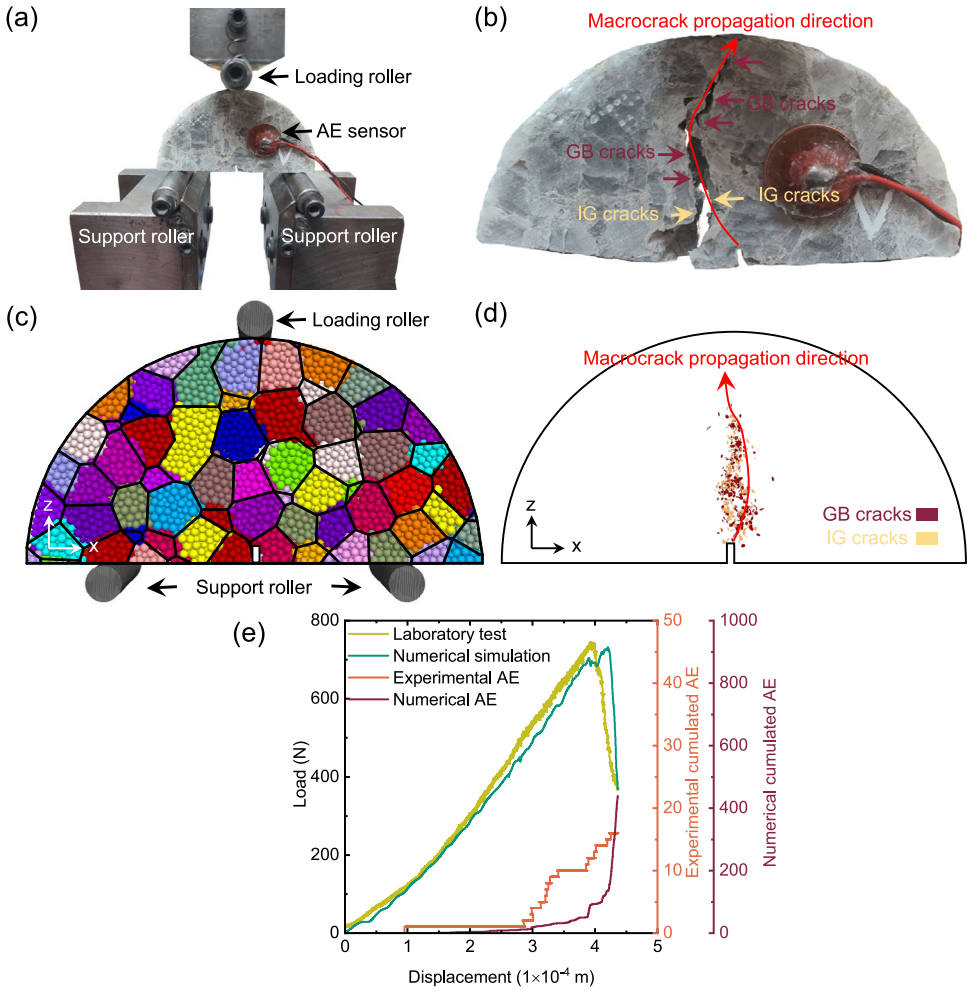

Fig. 4 Results of microparameters calibration. **a** and **b** show the experimental samples before and after loading; **c** and **d** show the numerical samples before and after loading; **e** Comparison of the load–displacement curves and the number of AE events obtained by numerical simulation and laboratory test

be regarded as conceptual representations that capture the general behavior of weathered selenite, rather than direct analogues of specific physical specimens.

3 Results

3.1 Influence of Weathering Degree on the Mechanical Properties and Microcracking Behavior

Numerous previous studies have explored the mechanical properties and microcracking behavior of rocks subjected to various degrees of weathering under different loading conditions (e.g., static uniaxial compression, dynamic loading), particularly in relation to processes such as chemical corrosion, wetting–drying cycles, and high-temperature treatment (Zhao et al. 2017; Lin et al. 2020; Moslehy et al. 2022). However, the tensile fracture behavior of weathered crystalline rocks under three-point bending conditions has received limited attention. This section presents a numerical investigation into the effects of weathering degree on the mechanical response and microcracking characteristics of modelled SCB selenite specimens. The analysis focuses on load–displacement responses, peak load, mode I fracture toughness, and the evolution of microcrack propagation patterns.

As the degree of weathering increases, the mechanical response of the modelled selenite samples undergoes notable changes. From slightly weathered to highly weathered conditions, the crack-closure stage becomes increasingly distinct (Fig. 6a). The SWS sample demonstrates an almost linear-elastic (or quasi-elastic) behavior throughout most of the loading process. Although a minor nonlinear region appears at the beginning of the load–displacement curve, this feature distinguishes it from entirely fresh and intact selenite. The initial generalized stiffness of the SWS sample (0.737 kN/mm) is approximately 64% lower than its

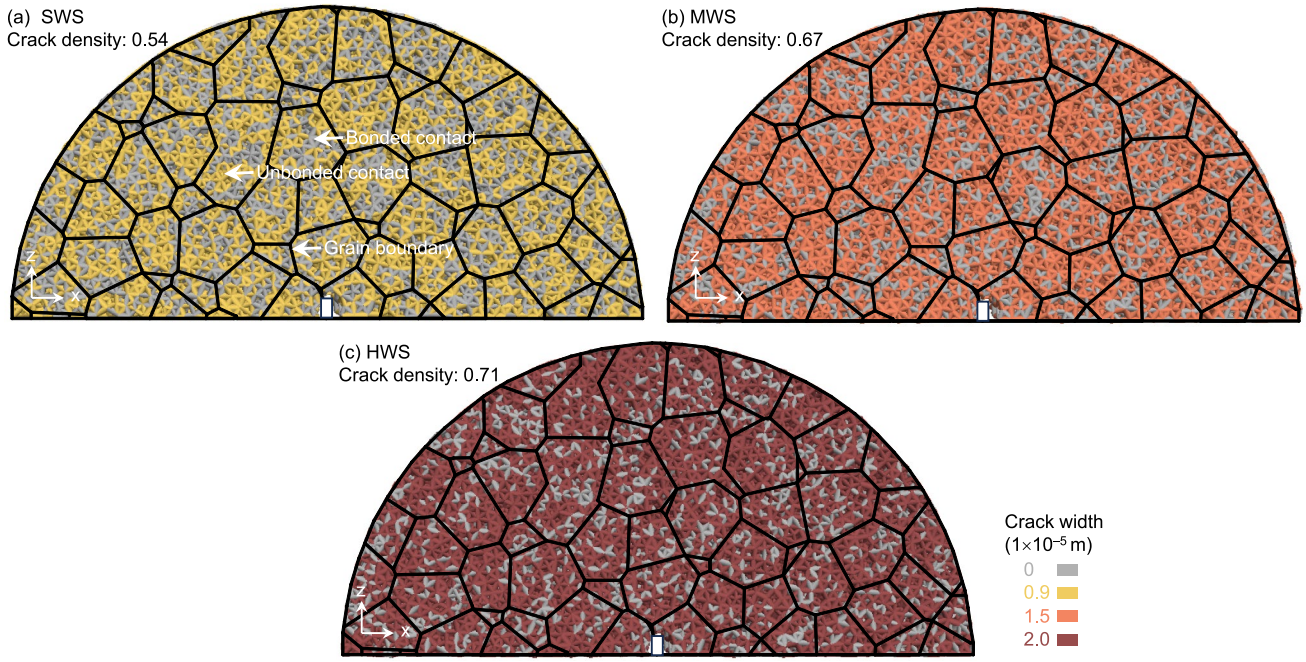

Fig. 5 Contact distribution of SCB selenite samples with three different weathering degrees. **a** SWS; **b** MWS; **c** HWS. Note: a crack width of zero indicates a bonded contact in the flat-joint model

stiffness measured at 50% of the peak load (2.061 kN/mm) (Fig. 6b). In the post-peak stage, the load drops abruptly, signifying a typical brittle failure mode. In contrast, the MWS sample exhibits a more pronounced strain-hardening behavior. Its initial generalized stiffness is considerably lower than that measured at 50% of peak load. Following the initial nonlinear stage, the response becomes nearly linear, transitioning into a strain-softening phase. The post-peak region is significantly more extended than that of the SWS sample. The HWS sample displays a deformation trend similar to that of the MWS sample, though with more apparent strain-hardening behavior in the early loading phase (Fig. 6a). In the post-peak stage, the load decreases gradually, indicating a transition from brittle to ductile failure.

Overall, with increasing weathering, the initial nonlinear (plastic deformation) stage becomes more pronounced (Fig. 6a), and the initial generalized stiffness decreases (Table 2). The mid-section of the load–displacement curves remains generally elastic across all weathering degrees, but the extent of the elastic region shortens with more advanced weathering. In contrast, both the initial strain-hardening segment and the final strain-softening segment become increasingly prominent as weathering progresses. These findings suggest that the increase in crack density and crack width induced by weathering (Fig. 5) significantly modifies the overall deformation behavior of selenite under three-point bending, influencing both pre-peak and post-peak responses. According to previous studies, an increase in crack density within flat-joint models leads to a reduction in the initial modulus, while a larger crack width extends the strain or displacement observed during the crack-closure stage (Peng et al. 2024). In the present work, both crack density and crack width vary as a function of weathering degree. Their combined effect induces distinct changes in the deformation behavior of the numerical models. These results more accurately reflect the natural weathering process in rocks, during which both microcrack density and width typically increase (Carroll 2012).

The mode I fracture toughness of the three modelled selenite samples was determined using Eq. (2), and the corresponding values are presented in Table 2. A clear decreasing trend in fracture toughness is observed with increasing weathering degree. For instance, the mode I fracture toughness of the HWS sample is 0.052 MPa·m$^{1/2}$, representing a reduction of approximately 71% compared to the SWS sample, which exhibits a value of 0.181 MPa·m$^{1/2}$. This degradation in fracture resistance is accompanied by an increase in the displacement at peak load and a decrease in the initial generalized stiffness, as shown in Table 2. These trends are consistent with previous observations of rock behavior under uniaxial compression, where increased weathering typically leads to reduced stiffness and enhanced deformability (Gupta and Rao 2000).

One distinct advantage of the 3D-GBM technique is its capability to quantitatively track the evolution of various

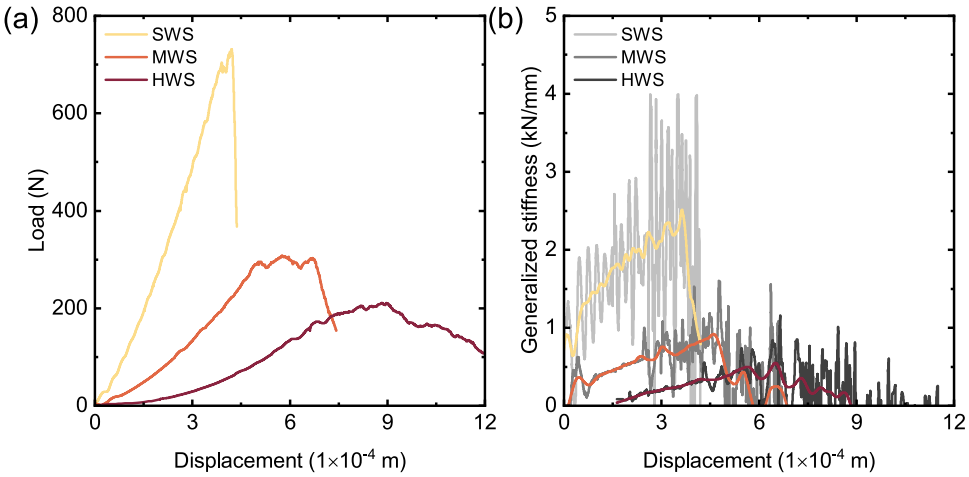

Fig. 6 **a** Load–displacement curve; **b** Generalized stiffness–displacement curve

Table 2 Mechanical properties of selenite with three different weathering degrees

Mechanical properties	SWS	MWS	HWS
Peak load (N)	731.5	308.16	211.07
Displacement at peak load (1×10^{-4} m)	4.21	5.75	8.82
Initial generalized stiffness (kN/mm)	0.737	0.316	0.106
Generalized stiffness at elastic stage (kN/mm)	2.061	0.698	0.359
Mode I fracture toughness (MPa·m$^{1/2}$)	0.181	0.076	0.052

microcrack types during loading. Figure 7 presents the load–displacement curves of the three modelled selenite samples with different degrees of weathering under mode I loading, alongside the evolution of four microcrack types (GBT, IGT, GBS, and IGS). Among these, tensile cracks (GBT and IGT) are predominant, with GBT cracks alone comprising over 50% of the total (Fig. 7d). This dominance of tensile failure is primarily attributed to the geometric configuration and loading conditions inherent to the SCB specimen. Furthermore, the pronounced occurrence of GBT cracking is closely linked to the presence of clay-rich cementing materials along grain boundaries, which deteriorate considerably during the weathering process. As weathering progresses, the mechanical integrity of these boundaries weakens, rendering them more susceptible to GBT-type cracking under external loading. The evolution of crack numbers exhibits distinct patterns across the three weathering levels. In the modelled SWS sample, only a few cracks are generated before peak load; however, the number increases rapidly during the peak and post-peak stages, indicating a quasi-brittle failure mechanism (Fig. 7a). In contrast, for the modelled MWS and HWS samples, crack initiation begins earlier at approximately 50% of the peak load with a marked increase observed between 70 and 80% of the peak load (Fig. 7b and c). Crack development continues well into the post-peak stage in both MWS and HWS samples. Another noteworthy observation is the timing of crack initiation among the different crack types. In the SWS sample, all four crack types tend to emerge almost simultaneously. However, in both MWS and HWS samples, GBT cracks initiate earlier than the others. This behavior highlights the increasing role of weathering-induced degradation at the grain boundaries, which accelerates failure in highly weathered crystalline rocks by promoting early tensile cracking along weakened interfaces.

The microcrack characteristics of both experimental and modelled SWS samples are compared in Fig. 8. In the modelled SWS sample, macro-scale tensile rupture develops through the initiation, propagation, and coalescence of intragrain and grain boundary cracks. The resulting fracture surface is irregular and strongly influenced by the intrinsic microstructure of selenite (Fig. 8a). This behavior is typical of crystalline selenite, where the mineral grains, primarily composed of gypsum, possess higher mechanical strength than the grain boundaries, which are often weakened by clay-rich cementing materials. Additionally, gypsum has one perfect cleavage plane, along which it is particularly prone to failure (Fig. 8e). Because the 3D-GBM adopted in this work does not explicitly represent the cleavage properties of gypsum, the experimental SWS samples exhibit more diverse and complex microcrack patterns (Fig. 8b-e). Nevertheless, grain boundary cracks are observed in both experimental and numerical results (Fig. 8a and b). The 3D-GBM approach enables detailed classification of microcracks into tensile and shear modes based on their failure mechanisms (Fig. 8f). In the experimental samples, lamellar cleavage cracks and transverse fractures are frequently observed due to the cleavage tendency of gypsum (Fig. 8c). Fragmented grains resulting from the coalescence of intragrain cracks appear in regions of high microcrack density (Fig. 8d and g). Microcrack localization is evident and serves as a

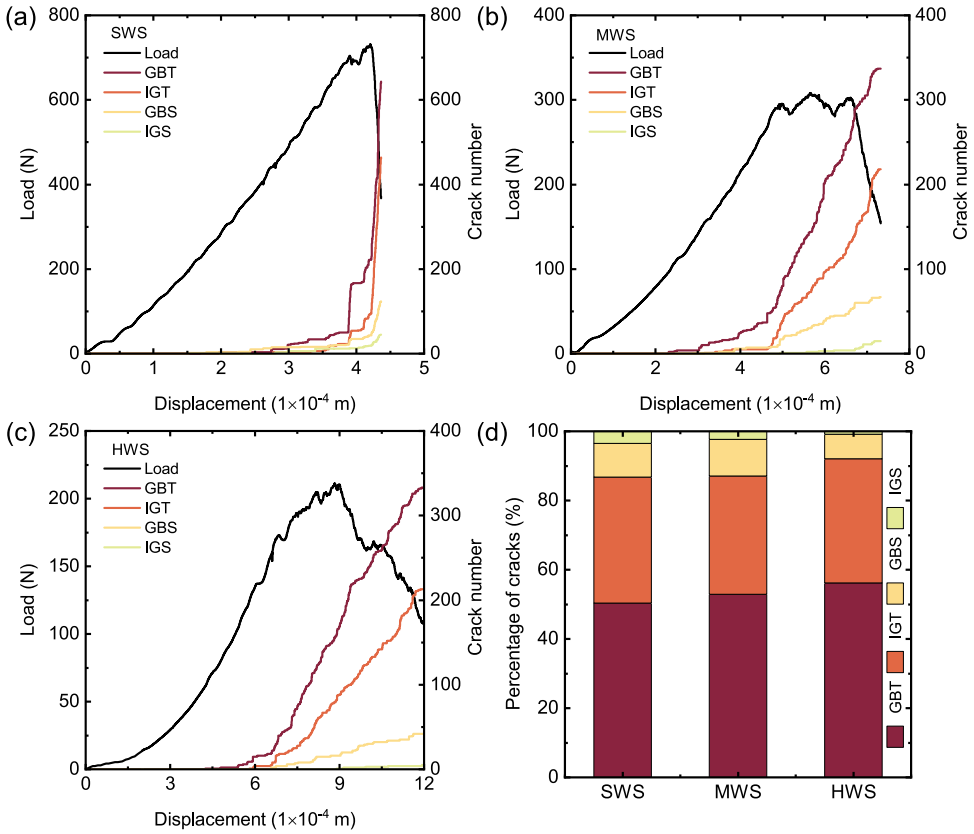

Fig. 7 The influence of weathering degree on the number of microcracks. **a** SWS; **b** MWS; **c** HWS; **d** Percentages of the four types of microcracks in three modelled SCB selenite samples

precursor to strain localization, which ultimately leads to the formation of macro-scale tensile fractures (Fig. 8b and g). Compared to other numerical approaches, grain-based modelling techniques offer significant advantages in simulating the failure mechanisms of crystalline rocks, particularly in capturing the initiation, propagation, and interaction of grain-scale microcracks (Li et al. 2020; Hu et al. 2024a; Bu et al. 2025; Zhou et al. 2025). For weathered crystalline rocks, the 3D-GBM, when integrated with the flat-joint model, effectively simulates the evolution of pre-existing microcracks induced by weathering, while preserving the inherent crystalline microstructure. Unlike fresh intact specimens, weathered rocks typically display more progressive and ductile-like failure behaviors, such as pronounced microcrack localization. This behavior is primarily attributed to the mechanical degradation of grain boundaries and the accumulation of defects introduced during the weathering process.

3.2 Influence of Weathering Degree on the Force Chain Distribution

The macroscopic mechanical behavior of selenite is strongly influenced by micromechanical processes occurring at the grain scale, driven by its inherently heterogeneous microstructure. This results in a multiscale mechanical response that transitions from microscale phenomena to macroscale manifestations. In crystalline rocks, the interlocking of mineral grains presents significant challenges in quantifying and visualizing force transmission under external loading. The evolution of force chain networks plays a critical role in understanding the mechanical response and damage progression in such materials (Zhang et al. 2017). Due to the difficulty of directly measuring contact forces in loaded crystalline rocks, GBMs have become a widely used tool for investigating these internal mechanisms in three dimensions.

Figure 9 shows the force chain distributions in modelled SCB selenite samples with varying degrees of weathering at different loading stages. In the visualization, both the thickness and color of contacts represent the magnitude of the contact force, with thicker and warmer-colored contacts corresponding to higher force magnitudes. To facilitate clearer visualization, a maximum contact force range of 0–5.0 N was uniformly applied across all samples. This range effectively captures the heterogeneous distribution of force chains throughout the loading process. Weathering degree has a significant influence on the spatial distribution and intensity of force chains (Fig. 9). In all modelled samples, the distributions are inherently heterogeneous due to the presence of microstructural discontinuities and pre-existing microcracks. The pre-existing microcracks in modelled weathered selenite are represented by unbonded contacts in the flat-joint model,

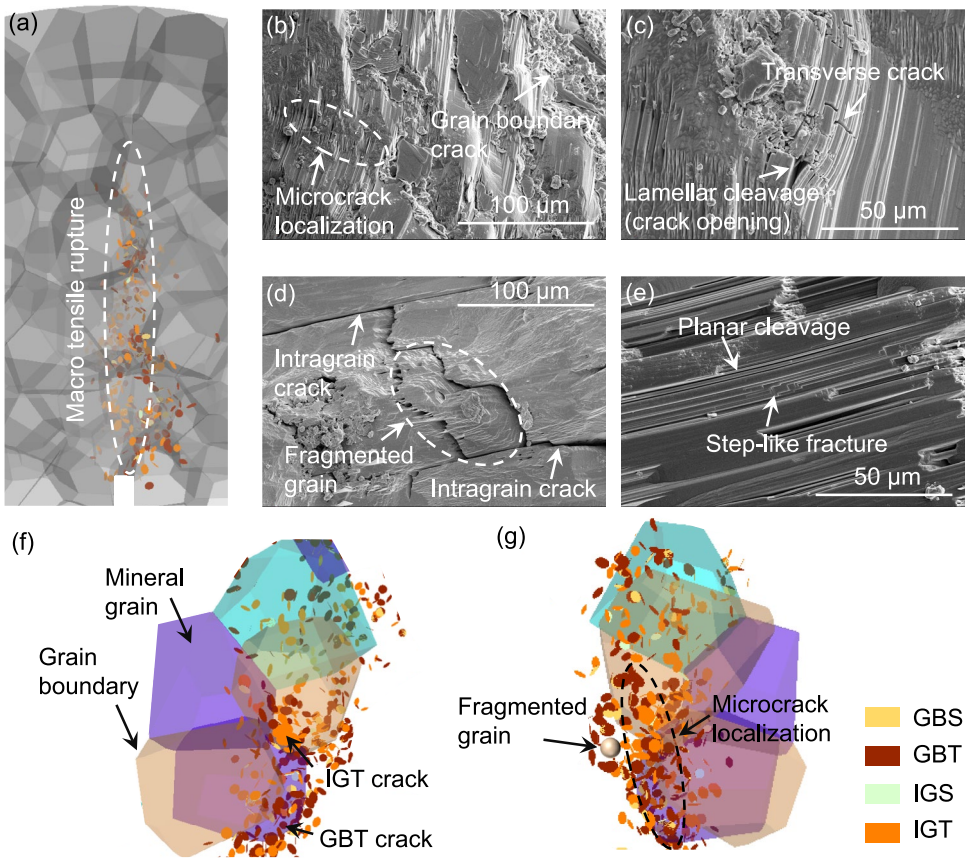

Fig. 8 Experimental and numerical observations of microcrack behavior. **a** fracture surface of SWS sample under mode I loading; **b** microcrack localization; **c** Lamellar cleavage and transverse cracks; **d** Fragmented grain; **e** Planar cleavage and step-like fracture; **f** Simulated IGT and GBT crack in 3D-GBM; **g** Simulated fragmented grain and microcrack localization in 3D-GBM

which are only capable of transmitting very low forces. In contrast, the primary load-bearing framework consists of bonded contacts. With increasing weathering degree, fewer load-bearing contacts (indicated by pink to deep red colors in Fig. 9) support the majority of the applied load, while the majority of contacts (shaded in blue) carry only minimal forces.

A key distinction among the weathering levels lies in the spatial organization of high-magnitude contact forces. In the SWS sample, load-bearing contacts are relatively homogeneously distributed (Fig. 9a). In contrast, in the HWS sample, high-force contacts appear sparse and highly unevenly distributed, both before and after peak load (Fig. 9c). This uneven distribution results from the random assignment of unbonded contacts in the simulation (Fig. 5), and contributes to a more heterogeneous internal stress field. Such heterogeneity promotes the initiation of force-induced microcracks during loading. The load levels at which the first microcracks appear in the SWS, MWS, and HWS samples are 196.48 N, 96.61 N, and 61.33 N, respectively (Fig. 7). This more heterogeneous force chain pattern enhances stress concentrations at localized sites, facilitating microcrack nucleation, propagation, and coalescence. Since all contacts were assigned identical strength values (Table 1), the differences in mechanical response arise primarily from the distribution of contact forces. The HWS sample, characterized by its sparse and irregular force chain structure, exhibits the lowest peak load and most pronounced plastic deformation behavior (Fig. 6 and Table 2). From a contact-force perspective, the unique geometry and loading configuration of the SCB specimen cause compressive forces to dominate near the loading and support points, while tensile forces prevail in the fracture process zone near the notch tip. Given that the tensile strength of rock is substantially lower than its compressive strength (Hoek and Martin 2014), it is reasonable that tensile failure dominates in this configuration (Fig. 7d).

3.3 Influence of Weathering Degree on the Acoustic Emission Characteristics

3.3.1 Localization of AE Events

AE, generated by the rapid growth of microcracks, is a ubiquitous phenomenon associated with brittle fracture and has proven to be an invaluable tool for understanding failure processes in rock materials (Lockner 1993). The AE technique enables the localization of microcrack activity within rock specimens using AE localization algorithms. Accurate

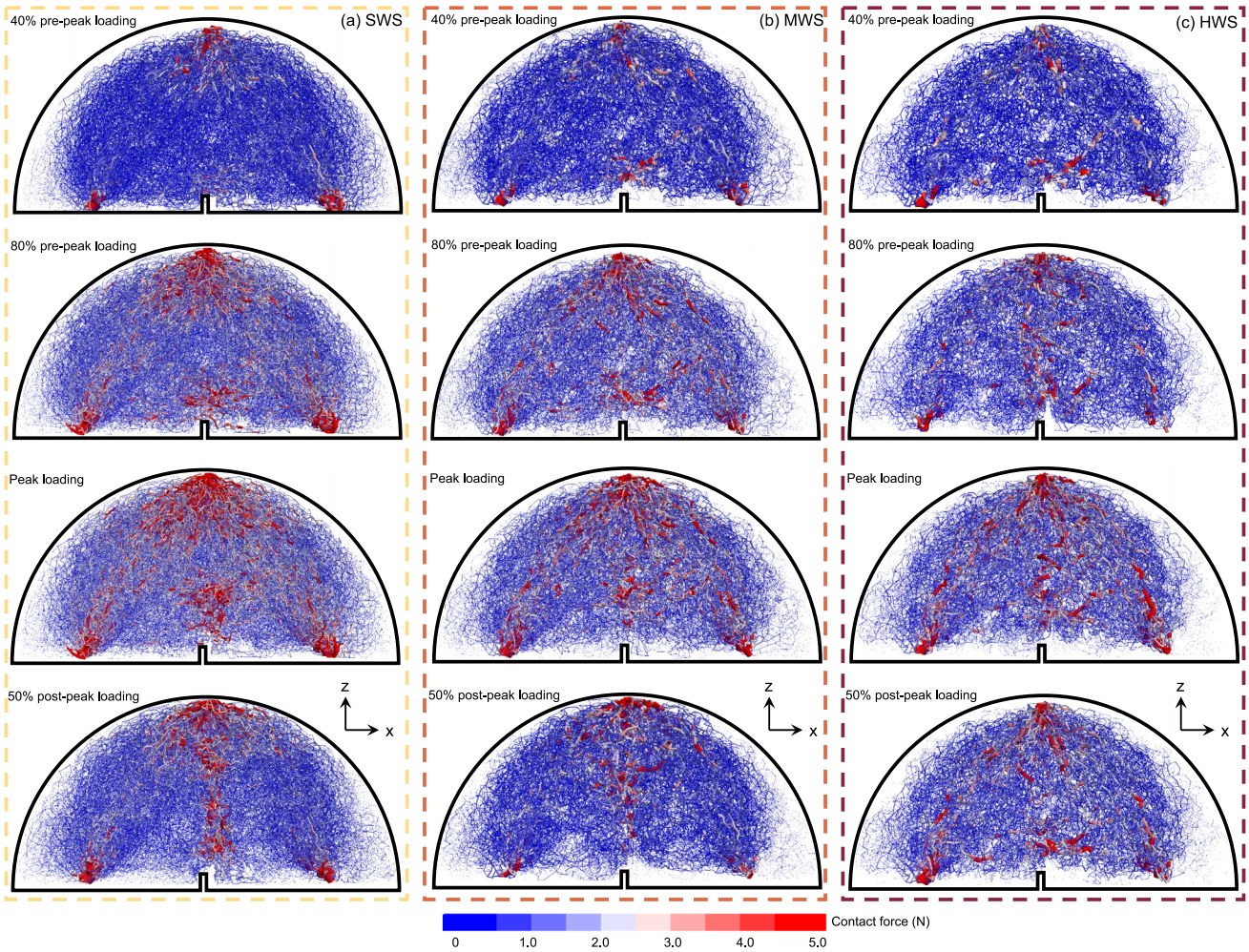

Fig. 9 Influence of weathering degree on the force chain distribution. **a** SWS; **b** MWS; **c** HWS. For visualization purposes, the force chain distribution is shown only from the *x*–*z* plane view. Note: thicker and redder lines represent larger contact forces, while thinner and bluer lines indicate smaller contact forces

localization of AE events is crucial for elucidating fracture mechanisms and for predicting potential failure zones. However, precise localization in laboratory settings remains a significant challenge. This difficulty arises primarily from the limitations of many AE localization algorithms, which often rely on simplifying assumptions that do not reflect the highly heterogeneous wave velocity fields present in rock. These velocity heterogeneities result from internal defects, grain-scale heterogeneities, and mineral inclusions (Weng et al. 2023). Moreover, constructing an accurate wave velocity model is inherently difficult due to the invisible nature of internal discontinuities and the complexity of their spatial distribution.

In this work, the 3D-GBM was employed to simulate AE behavior during the loading of rock specimens, based on moment tensor theory (Hazzard and Young 2000, 2004). Unlike conventional experimental methods, this numerical approach benefits from precisely defined microcrack locations, offering a distinct advantage in the localization accuracy of AE events. The spatial localization of AE events in modelled SCB selenite samples with varying degrees of weathering was investigated using the 3D-GBM (Fig. 10). At early loading stages, such as 80% of the pre-peak load, AE events are concentrated near the notch tip. As loading progresses toward the peak, AE activity propagates upward in the direction of the loading point. By the 50% post-peak stage, AE events become widely distributed within a three-dimensional region along the maximum tensile stress plane, which extends from the notch tip toward the loading point (Fig. 10). Mechanically, under mode I loading conditions, fractures tend to initiate at the notch tip and propagate linearly toward the load application point, following the direction of maximum tangential stress (Wei et al. 2017; Alneasan and Behnia 2021). With increasing weathering, the spatial distribution of AE events becomes progressively more dispersed. This trend is closely linked to the changing

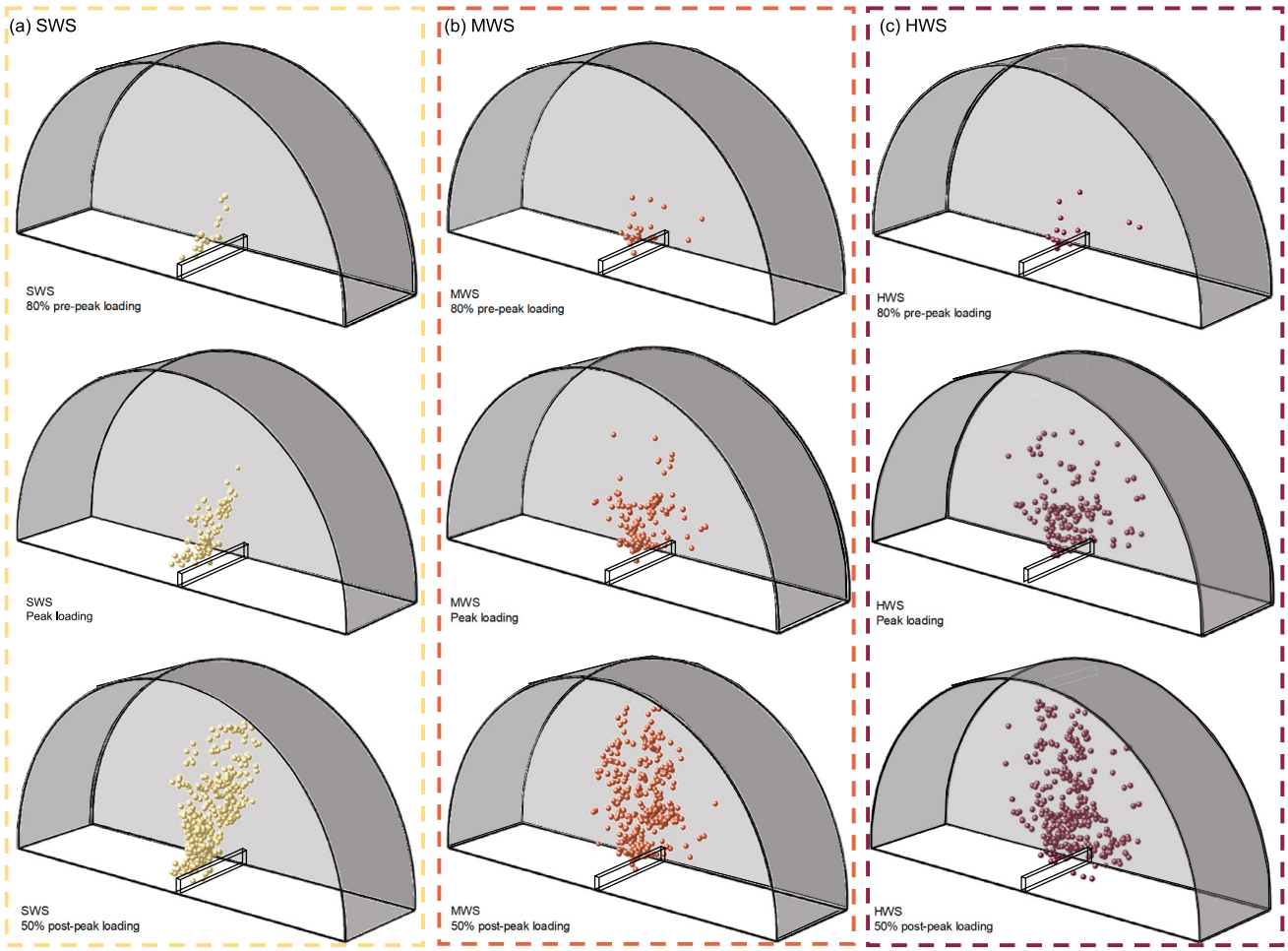

Fig. 10 Localization of AE events of selenite SCB samples under mode I loading. **a** SWS; **b** MWS; **c** HWS

internal force chain distributions within the samples (Fig. 9). In the SWS sample, AE events are largely confined to a well-defined fracture plane oriented approximately parallel to the *z*-axis (Fig. 10a). These numerical results are consistent with experimental observations in fresh or slightly weathered rocks (Guo and Zhao 2022; Wang et al. 2024b). By contrast, in the HWS sample, AE events are scattered irregularly throughout the region between the notch tip and the loading point, making it difficult to distinguish a clear fracture surface (Fig. 10c). This behavior resembles the failure patterns observed in fresh granite SCB samples, where grain boundary heterogeneity significantly influences fracture development under mode I loading (Hu et al. 2024a).

The presence of numerous pre-existing microcracks, pores, and other microstructural defects in highly weathered crystalline rocks makes it substantially more difficult to construct an accurate wave velocity field than in fresh, intact specimens. Consequently, experimental AE localization becomes increasingly unreliable under such conditions. In this context, the 3D-GBM approach presented in this work provides a valuable alternative. By realistically capturing the microstructural characteristics of weathered crystalline rocks, it offers a robust and accurate framework for analyzing AE event localization and the associated fracture evolution.

Based on the above analysis, the spatial localization of AE events in selenite SCB samples varies significantly with the degree of weathering. As a non-parametric statistical tool, kernel density estimation (KDE) is capable of constructing the probability density function of AE event distributions within a given sample. This method has been widely adopted to investigate the localization characteristics of AE events in brittle materials (Lopez-Comino et al. 2017; Teng et al. 2023; Yu et al. 2024). In this study, KDE was employed to generate contour maps of AE event distributions for weathered selenite samples at different loading stages (Fig. 11). All AE events were visualized using a Gaussian kernel function, where regions of higher event density are indicated by

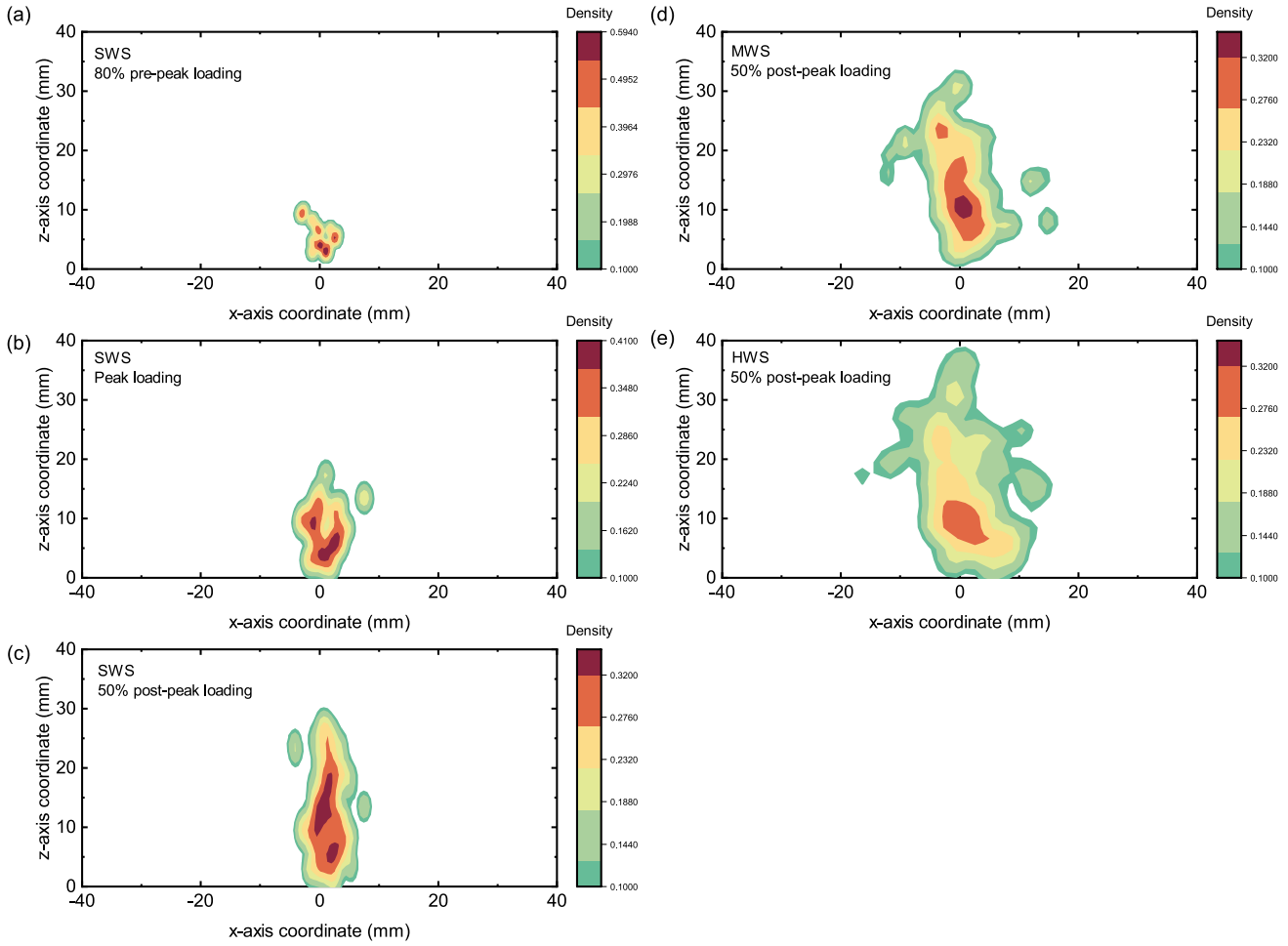

Fig. 11 The kernel density estimation of AE events. **a** SWS at 80% pre-peak loading; **b** SWS at peak loading; **c** SWS at 50% post-peak loading; **d** MWS at 50% post-peak loading; **e** HWS at 50% post-peak loading

deep pink, and areas of lower density are marked by lime green. The KDE maps illustrate the probability density of AE events projected onto the *x*–*z* plane, highlighting their spatial evolution across samples with varying weathering degrees.

The AE events exhibit a certain degree of aggregation and spatial regularity. The location of the maximum density, as determined by KDE, is generally considered indicative of the most rapidly developing crack zone (Teng et al. 2023). In the modelled SWS sample, the maximum density point progressively shifts from the notch tip toward the loading point as the load increases, reflecting crack propagation under increasing stress (Fig. 11a-c). These maximum density points are primarily aligned within a plane parallel to the *z*-axis, a feature typical of brittle failure. At the 50% post-peak loading stage, AE events are more uniformly distributed within a concentrated failure zone. The maximum density region continues to propagate forward from the notch tip, forming a well-defined damage accumulation zone (Fig. 11c). Notably, the region from $x = -5$ mm to $x = +5$ mm is almost entirely covered by a large soft red density field, reflecting the progressive accumulation of micro-damage. This distribution correlates well with the macroscopic fracture propagation observed in both numerical and experimental results (Fig. 4). The evolution of density fields and the movement of maximum density points provide a clear visual representation of damage development in the SWS sample and closely correspond to the observed crack growth path.

In contrast, the KDE distributions for the MWS and HWS samples (Fig. 11d and e) are markedly different. AE events in these samples are dispersed across a wider area in the *x*–*z* plane, indicating the formation of multiple secondary micro-fracture planes. These dispersed fracture planes coalesce to form a broader damage zone, which ultimately leads to specimen failure. This behavior is characteristic of ductile failure modes. Both the accurate 3D localization of AE events (Fig. 10) and the KDE distributions in the *x*–*z*

plane (Fig. 11) clearly demonstrate the significant influence of weathering on the spatial characteristics of AE activity in selenite samples under mode I loading. The results reveal a consistent transition from brittle failure, dominated by a single planar fracture (Figs. 10a and 11c), to ductile failure, marked by the development of multiple interacting fracture planes forming a damage zone (Figs. 10b, c, 11d and e), as the weathering degree increases. This transition highlights critical changes in the mechanical behavior of weathered crystalline rocks and underscores the need for spatially resolved AE analysis in laboratory testing.

For laboratory-scale investigations, these findings underscore the importance of integrating 3D AE localization with statistical density analysis to better capture the complex fracture processes associated with rock weathering. Additionally, they highlight the limitations of traditional AE localization techniques in highly weathered rocks, where strong internal heterogeneity violates assumptions of material homogeneity and simple fracture propagation paths. In this context, advanced numerical modeling approaches, such as grain-based simulations, provide a powerful tool for replicating and analyzing the progressive damage processes observed in naturally weathered rock masses. These models are particularly valuable in situations where conventional continuum-based methods are unable to capture the complex and evolving failure mechanisms of heterogeneous materials.

3.3.2 Magnitude and *b*-Value

The magnitude M reflects the rupture strength and energy released during an AE event. It is important to note that the moment magnitude formulation used here (Eq. (5)) is derived from the moment magnitude scale commonly applied in seismology. This uniform magnitude model is well suited for the statistical analysis of various magnitude scales and is widely employed to characterize the fracture strength of AE events at the laboratory scale (Hazzard and Young 2000, 2004).

Figure 12 illustrates the spatial distribution of AE events and their corresponding magnitudes in the x–z plane for the three modelled selenite samples with different degrees of weathering. Differences in the localization patterns of AE events among these samples have been discussed previously (Figs. 10, 11). More notably, the AE magnitudes also vary significantly, reflecting distinct levels of energy release during fracturing in each sample. For example, in the SWS sample, a cluster of high-magnitude AE events is concentrated near $x = 0$ mm, with several events reaching a maximum magnitude of approximately − 6.56 (Fig. 12a). This indicates intense energy release associated with the catastrophic failure observed in the SWS sample. In contrast, the MWS and HWS samples exhibit a more dispersed distribution of lower-magnitude AE events, with maximum magnitudes near − 7.00 (Fig. 12b and c). These variations in magnitude distribution correspond closely with the load–displacement behavior of the samples, where the SWS shows brittle failure characteristics, while the MWS and HWS display ductile failure features (Fig. 6).

The distinction in failure behavior among the weathered selenite samples is further illustrated by the load–displacement and magnitude–displacement curves (Fig. 13). In the SWS sample, the pre-peak stage is characterized by sporadic AE events of low to moderate magnitude ($M < -6.8$). However, at peak and post-peak loading stages, a rapid succession of AE events occurs, including several high-magnitude events (Fig. 13a). This reflects a significant release of energy associated with catastrophic failure. In contrast, the MWS and HWS samples exhibit abundant low-magnitude AE events distributed over approximately 50% of both pre-peak and post-peak stages, indicative of a failure process dominated by numerous low-energy fracturing events, consistent with ductile failure behaviour (Fig. 13b and c).

To further clarify the influence of weathering on magnitude distribution, a homogeneous selenite (HS) sample was introduced for comparison. This model assumes fully bonded contacts without pre-existing microcracks, representing fresh and intact selenite. All other micro-parameters were kept consistent with the SWS model (Table 1). The magnitude distribution of AE events in the HS sample is distinctly different from those in the weathered samples (Fig. 13d). The HS sample generates fewer AE events overall, but with generally higher magnitudes, reaching a maximum magnitude of approximately − 5.45, which is substantially greater than the maxima observed in the weathered samples. Conversely, the weathered samples show progressively lower maximum and average magnitudes with increasing weathering degree, reflecting a reduction in failure intensity. Furthermore, AE events were classified into tensile, shear, and implosive types based on Eq. (7) (Fig. 13a-c). Tensile events dominate all samples, consistent with the predominance of tensile microcracking in selenite under mode I loading. Shear events occur less frequently, likely due to the layered mineral structure of gypsum, which inhibits frictional sliding. Implosive events, although the least common, provide important insight into internal collapse mechanisms. Notably, implosive events in the SWS sample appear exclusively in the post-peak stage, indicating their association with rapid structural failure and localized compaction following macrocrack propagation. In the PFC modeling framework, implosive events primarily consist of micro tensile cracks, but the surrounding particles move inward to fill the voids created by tensile cracking (Hazzard and Young 2000, 2004). This explains why most implosive events occur in the post-peak stage for the SWS sample, where macro tensile cracks cause inward particle displacement to compensate for volume changes (Ma et al. 2020).

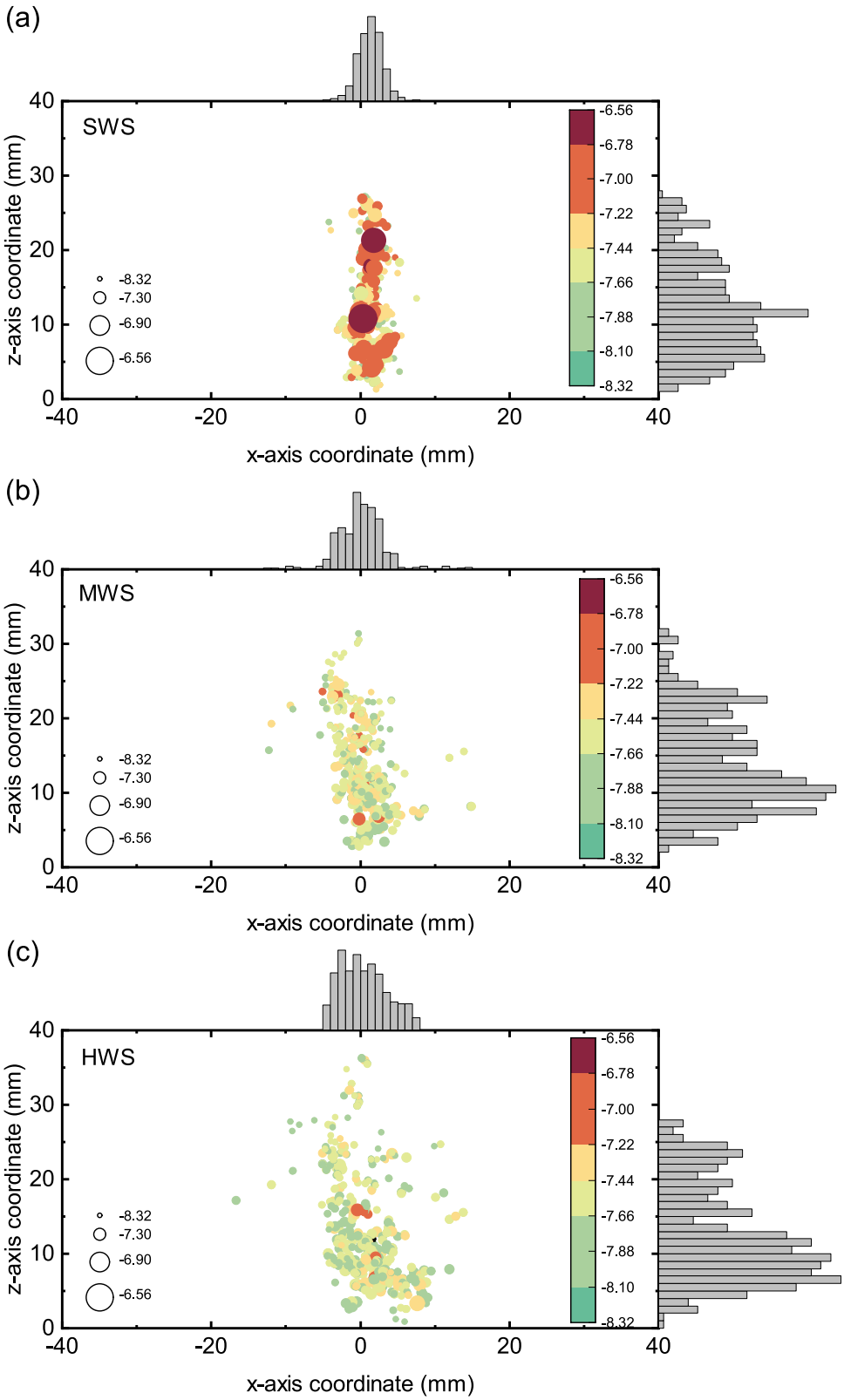

Fig. 12 Localization of AE events at the *x*–*z* plane and their corresponding magnitudes. **a** SWS; **b** MWS; **c** HWS. Note: histograms showing the number of AE events along the *x* and *z* directions are displayed above and to the right of the subplots, respectively

In contrast, the MWS and HWS samples, which contain more and wider pre-existing microcracks modeled by unbonded contacts within the flat-joint model (Fig. 5), exhibit implosive events during both pre-peak and post-peak stages (Fig. 13b and c). The earlier onset and increased frequency of implosive events in these samples can be

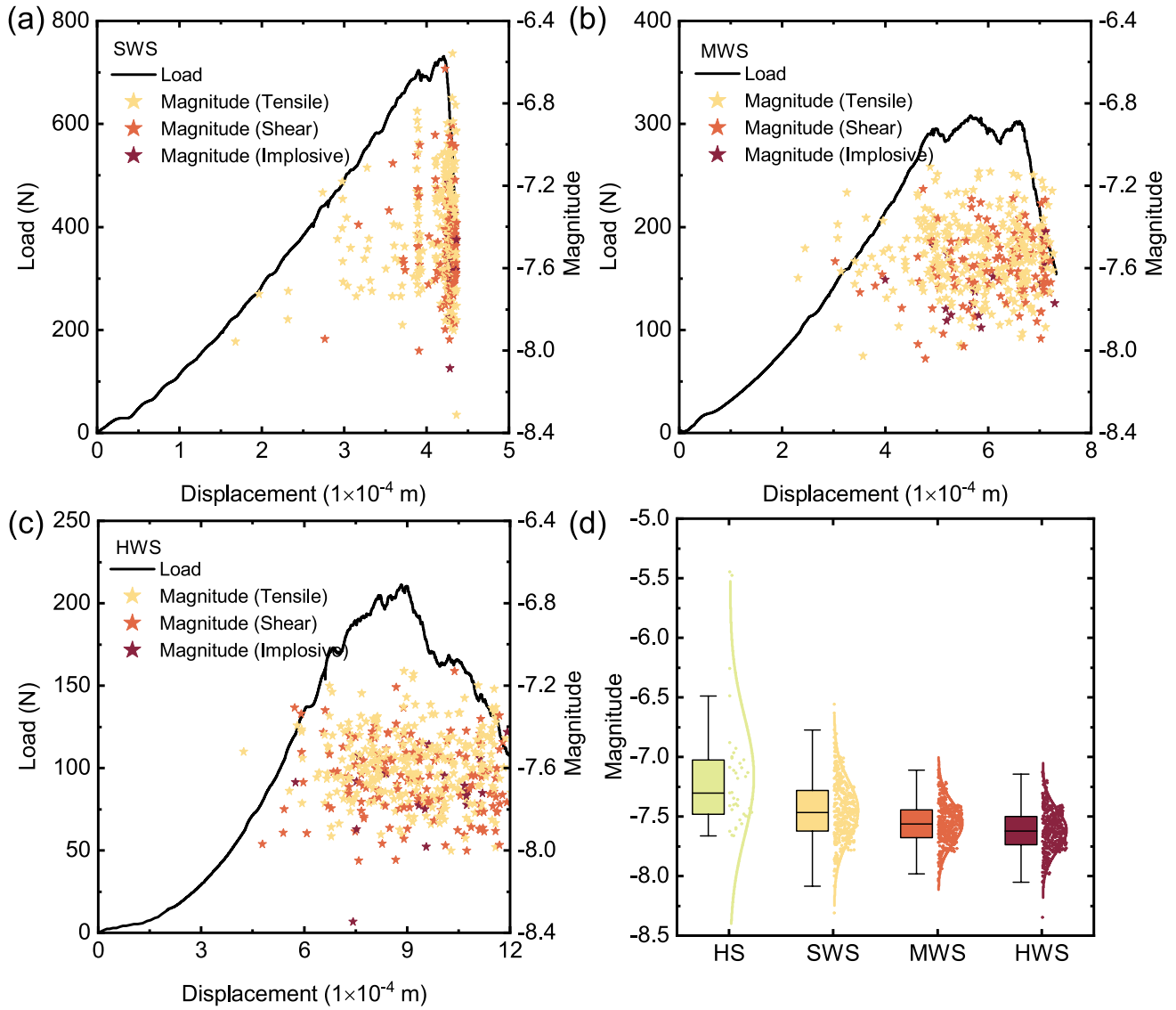

Fig. 13 Load–displacement curve and corresponding magnitude-displacement distribution. **a** SWS; **b** MWS; **c** HWS; **d** Magnitude distributions of AE events for four modeled selenite samples under mode I loading. The color of the pentagrams in (**a**), (**b**), and (**c**) indicates the source types of the AE events

attributed to greater microstructural degradation caused by weathering, which facilitates progressive pore closure and internal collapse under loading.

In summary, the degree of weathering exerts a significant influence on the spatiotemporal characteristics of AE events, including their magnitude distribution and source mechanisms. Slightly weathered selenite (e.g., SWS sample) exhibits brittle and localized failure, characterized by concentrated high-magnitude AE events and post-peak implosive activity along a dominant fracture plane. In contrast, moderately and highly weathered samples (e.g., MWS and HWS samples) display ductile and distributed deformation, marked by lower, more uniformly distributed AE magnitudes and a wider temporal range of implosive events. These results underscore the critical role of microstructural degradation in governing the macroscopic mechanical behavior of weathered crystalline rocks.

The *b*-value quantifies the relative frequency of low- versus high-magnitude AE events and is derived from the Gutenberg-Richter relationship (Gutenberg and Richter 1944). Its magnitude is closely linked to the stress state at the AE source and the scale of crack rupture (Lockner 1993; Liu et al. 2020; Sun et al. 2025b). A decreasing *b*-value indicates a lower proportion of small-magnitude AE events and a relative increase in the frequency of larger events, often associated with the development of more severe fractures. Conversely, an increasing *b*-value reflects a predominance of smaller events, suggesting that

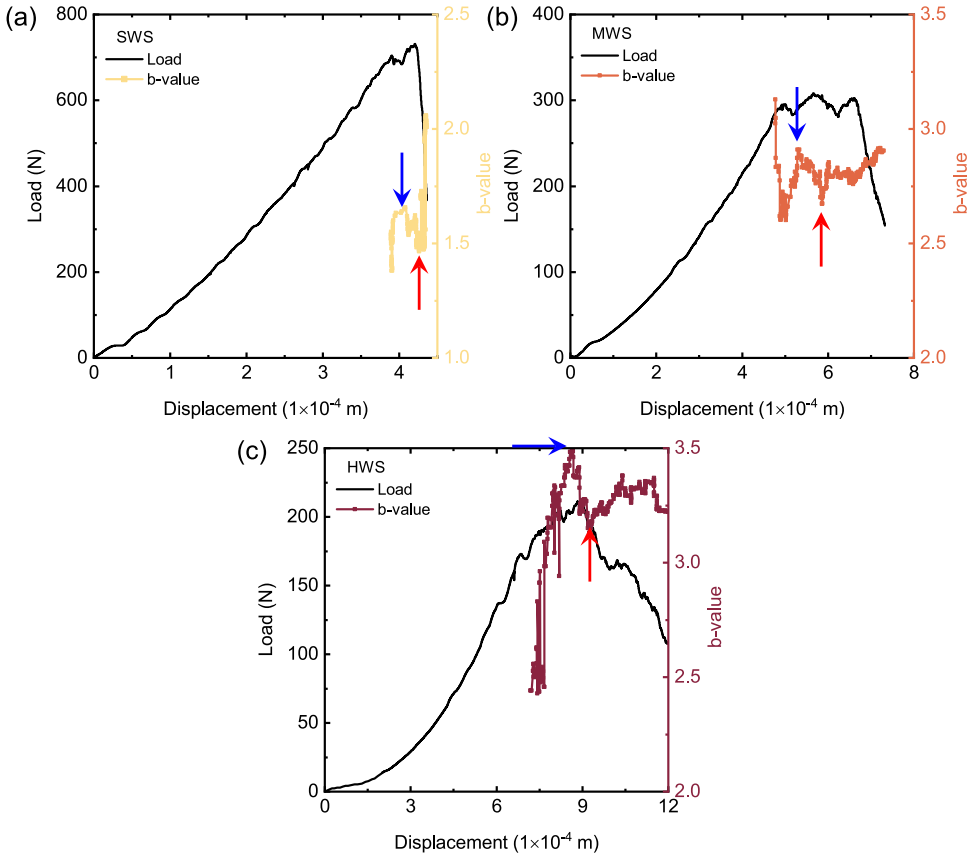

Fig. 14 Evolution of *b*-value for three weathered selenite SCB samples under mode I loading. **a** SWS; **b** MWS; **c** HWS. Note: the blue solid arrow and the red solid arrow indicate the start and end points of the rapid drop in *b*-value, respectively

the rock fracture process is dominated by micro- to meso-scale cracking.

In this work, *b*-value computation begins from the 50th recorded AE event, with each subsequent value calculated cumulatively by incorporating all AE events generated up to that point. The overall *b*-values for the SWS, MWS, and HWS samples are 2.01, 2.91, and 3.22, respectively. The detailed temporal evolution of the *b*-values is presented in Fig. 14a-c. Although the three weathered selenite models were all developed using the same 3D-GBM and share identical grain-size distributions and mineral compositions (Fig. 3), they differ in the density and width of pre-existing microcracks, represented by unbonded contacts within the flat-joint model (Fig. 5). These differences result in heterogeneous deformation responses among the samples, leading to variations in fracture scale under loading.

The HWS model, which contains a greater number of pre-existing microcracks, tends to generate a higher proportion of small-scale fractures. This is reflected in the AE magnitude distribution, where numerous low-magnitude events are observed (Fig. 13c). In contrast, the SWS sample, which contains fewer and narrower microcracks, maintains a stronger overall bonding framework and shows a greater tendency toward larger-scale fractures, resulting in fewer but higher-magnitude AE events (Fig. 13a). Consequently, the *b*-value is highest in the HWS sample, followed by MWS, and lowest in SWS.

All three samples exhibit a sharp drop in *b*-value near the peak load, a transition that is highlighted in Fig. 14 by a solid blue arrow indicating the onset and a solid red arrow marking the end of this critical stage. This trend suggests that a declining *b*-value may serve as a reliable precursor to impending catastrophic failure in weathered selenite. Such behavior is consistent with observations from numerous experimental rock studies (Lei et al. 2004; Goebel et al. 2013; Muñoz-Ibáñez et al. 2021; Liu et al. 2020; Sun et al. 2025b).

3.3.3 Source Mechanism

The source mechanisms of AE events were analyzed using the Hudson diagram (Hudson et al. 1989), in which each moment tensor is transformed into the dimensionless parameters T and k (ranging from -1 to 1) based on Eq. (8) and Eq. (9). These parameters characterize the shear and volumetric components of the corresponding failure mechanisms. The Hudson diagram facilitates the statistical interpretation of dynamic cracking behavior across a large number of fracture events (Sun et al. 2023). The inversion results for AE events generated in the three modelled

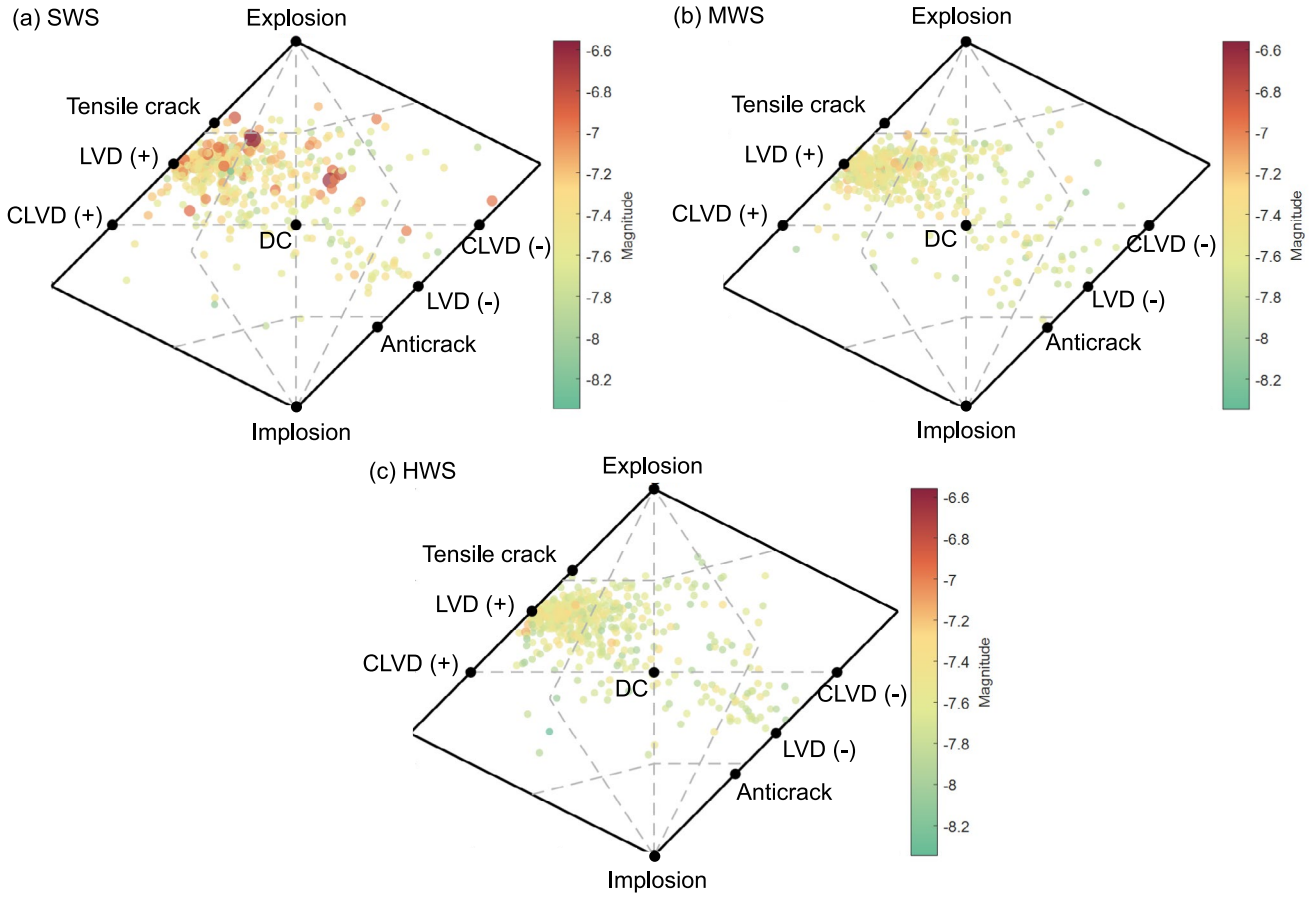

Fig. 15 Hudson diagram of AE events of three weathered selenite SCB samples under mode I loading. **a** SWS; **b** MWS; **c** HWS

weathered selenite samples under mode I loading conditions are presented in Fig. 15.

The results show that all three samples exhibit broadly similar distributions of AE source mechanisms, with most events clustering in the upper-left quadrant of the Hudson diagram. This region corresponds to tensile cracking with a positive LVD (+), which is consistent with the nature of mode I loading that predominantly induces opening-mode fractures. These observations indicate that tensile failure remains the dominant rupture mechanism across all weathering degrees. Interestingly, the SWS sample displays a more dispersed distribution of AE events compared to the MWS and HWS samples (Fig. 15a). While the majority of its AE events are still located within the LVD (+) region, several are positioned near the double-couple (DC) region and even extend toward the LVD (−) and CLVD (−) zones. This dispersion suggests the potential occurrence of localized shear or volumetric collapse events, possibly resulting from intrinsic microstructural heterogeneity or stress redistribution effects during crack propagation. In contrast, AE events in the MWS and HWS samples are more tightly concentrated within the tensile region, with only minor deviations toward other mechanism types (Fig. 15b and c). This pattern implies that, despite the presence of pre-existing microcracks and larger crack apertures in the more weathered rocks, the dominant fracture mechanism under pure tensile loading remains tensile in nature. It is also notable that, in the SWS sample, a small number of high-magnitude AE events are located near the DC region. This may be attributed to the modeling framework used in this work. The 3D-GBM explicitly incorporates grain boundaries and their mechanical interactions. Under heterogeneous stress fields (Fig. 9), these boundaries may serve as preferential zones for localized shear failure. When such failures involve higher energy release, their moment tensor solutions may project toward the DC region in the Hudson diagram.

Overall, the results suggest that AE source mechanisms in selenite under mode I loading are predominantly governed by the external loading configuration rather than the degree of internal degradation. While weathering clearly affects spatial AE localization, magnitude distribution, and *b*-value evolution, it does not appear to substantially alter the overall failure mode as determined from Hudson analysis under tensile loading conditions. However, under

more complex loading regimes such as uniaxial or triaxial compression, the degree of weathering is likely to exert a more pronounced influence on the resulting source mechanisms. Previous studies on rocks such as granite and sandstone have demonstrated that variations in microstructure can significantly impact AE source mechanisms under such stress states (Raziperchikolaee et al. 2021).

4 Discussion

Rock weathering is a multifactorial geological process that arises from the continuous interaction between physical and chemical mechanisms over geological timescales. Physically, processes such as repeated wetting–drying cycles, freeze–thaw action, and thermal fluctuations lead to mechanical breakdown through stress accumulation and microcrack development. Chemically, reactions including oxidation, hydrolysis, carbonation, and mineral dissolution progressively alter the mineralogical composition and weaken the cementation at grain boundaries. The combined action of these mechanisms not only modifies the microstructure and porosity of the rock matrix but also degrades its mechanical integrity, leading to progressive deterioration of strength and stiffness. These processes substantially influence the mechanical, lithological, and pore structure characteristics of rocks, forming an intricately coupled system (Nicholson 2001). Weathering can alter key physical properties such as density and porosity, as well as mechanical behaviors including strength, deformability, and failure modes (Gupta and Rao 2000). Stone cultural relics, which have been exposed to natural environments over centuries, are particularly vulnerable to environmental factors such as acid rain and temperature cycling (Lin et al. 2024; Liu et al. 2025; Sun et al. 2025a). As a result, these relics often exhibit varying degrees and types of weathering, ultimately compromising their long-term structural stability.

In this work, a 3D-GBM was employed to investigate the influence of weathering degree on the nonlinear deformation behavior and AE characteristics of a crystalline rock, selenite. The rock microstructure was realistically modeled using 3D Voronoi tessellation, while pre-existing microcracks induced by weathering were simulated through unbonded contacts within a flat-joint model. The results clearly show that the degree of weathering significantly affects both the deformation behavior and mode I fracture toughness of selenite. More importantly, distinct AE characteristics emerge as the weathering degree increases. Specifically, a higher degree of weathering corresponds to a progressive reduction in mode I fracture toughness (Fig. 16). Under mode I loading in SCB samples, the AE response also evolves with increasing weathering, including a higher *b*-value, a longer foreshock stage, reduced maximum AE magnitudes, and a shift in AE event spatial distribution from clustered to dispersed patterns (Fig. 16).

According to the results of this work, rock weathering leads to a notable increase in both the number and width of pre-existing microcracks, which substantially degrades the macroscopic mechanical behavior and strength of crystalline rocks. This underscores the fundamental role of microscale weakening, especially within mineral grain interiors and along grain boundaries, in controlling macroscopic deformation processes such as strain hardening, strain softening, and ultimate failure. The progressive deterioration of these microstructural features directly translates into reduced fracture resistance and mechanical stability at the macroscale. These findings offer mechanistic insight into the degradation of mechanical properties in weathered crystalline rocks and provide a basis for evaluating their structural integrity under natural or engineered loading conditions.

Importantly, the results of this work also carry implications for the preservation and structural assessment of stone-based cultural heritage. In southern China, especially in regions such as Sichuan and Chongqing, naturally occurring rainfall and groundwater are often weakly acidic. This chemical environment accelerates the dissolution of cementing agents between mineral grains in sandstone, weakening the cohesion and leading to a gradual decline in its load-bearing capacity (Lin et al. 2024). Additionally, the presence of clay minerals in such rocks introduces further vulnerability. When hydrated, these minerals swell, causing internal stress and microstructural degradation, which further compromise the stiffness and strength of rocks (Montes et al. 2004). These effects are particularly relevant for the protection of historical stone relics in southern China, such as grotto temples, stone steles, and carved rock facades, many of which have experienced prolonged exposure to weathering and environmental loading (Liu et al. 2025; Sun et al. 2025a). Given these vulnerabilities, the use of AE monitoring in heritage conservation requires region-specific calibration to account for local weathering conditions. AE signals must be interpreted in the context of weathering-induced heterogeneity in order to accurately assess the health status and damage evolution of stone monuments. This approach enhances the precision of early-warning systems and informs more targeted conservation strategies. Similar challenges are encountered in Europe. For example, the Garisenda Tower in Bologna, Italy, has recently exhibited signs of structural instability due to progressive weathering of its selenite-based foundation materials (Dallavalle et al. 2022). Uneven deterioration accumulated over centuries has made the base of the tower susceptible to differential settlement and tilting. In such cases, AE monitoring that accounts for the spatial distribution and severity of weathering damage can serve as an effective diagnostic tool, enabling timely preservation efforts and well-informed structural interventions.

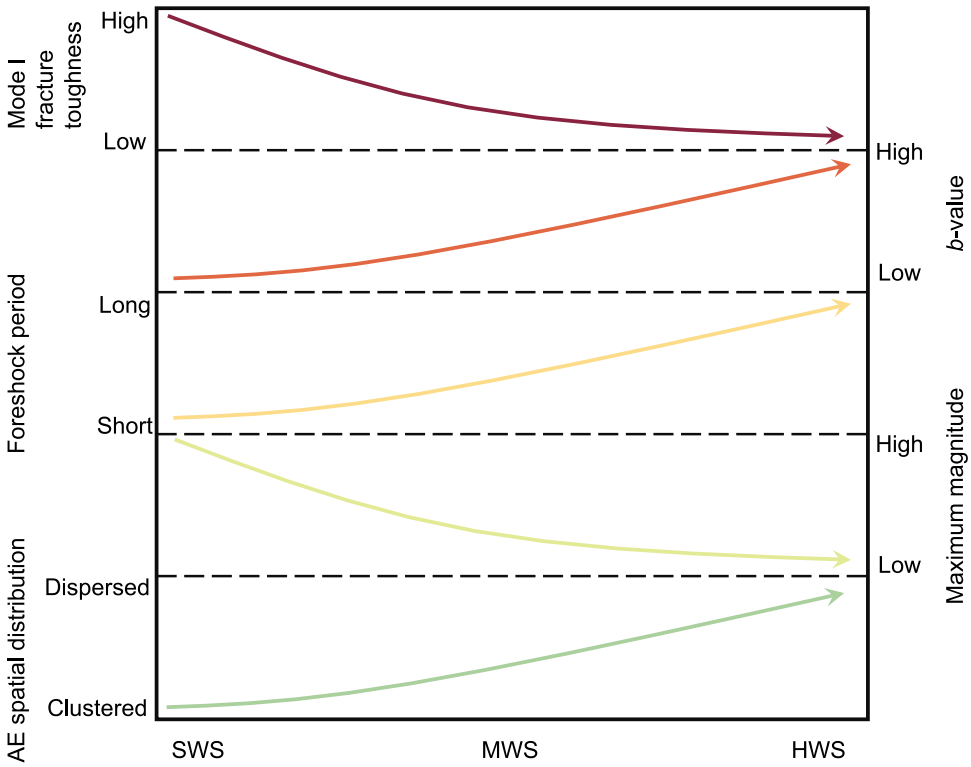

Fig. 16 Evolution trends of mechanical properties and AE characteristics of selenite SCB samples with three different weathering degrees under mode I loading

In conclusion, the integration of high-resolution numerical simulations with AE-based structural health monitoring, when calibrated against degrees of weathering, offers a robust framework for assessing the stability and deterioration of weathered rocks. This interdisciplinary approach is not only crucial for geotechnical and rock engineering applications but also plays an increasingly vital role in the conservation of culturally and historically significant stone structures. Collaboration among geomechanics researchers, heritage conservation experts, and monitoring engineers is essential to develop tailored solutions for long-term stability and risk mitigation in both natural and built environments.

Although the flat-joint model implemented within 3D-GBM in PFC has been employed to investigate the fracture processes in this work, several limitations remain. First, in the present work, only the presence of pre-existing microcracks resulting from physical weathering in weathered selenite rocks was considered. However, crystalline selenite rocks also undergo chemical weathering processes that alter mineral grains and lead to nonlinear mechanical responses. For example, the primary mineral in the selenite studied here is gypsum ($CaSO_4{\cdot}2H_2O$), which undergoes notable mineralogical changes under chemical weathering. The observed color change of selenite from gray to white is attributed to the formation of a mosaic of bassanite (semi-hydrate, $2CaSO_4{\cdot}H_2O$) and soluble anhydrite ($CaSO_4$) microcrystals (Dallavalle et al. 2022). These sulfate phases are highly unstable and tend to rehydrate rapidly back into gypsum by absorbing moisture and capillary water, ultimately forming an alabastrine texture. These mineral transformations are accompanied by significant volume changes, which can profoundly influence the rock microstructure and mechanical behavior. However, the current 3D-GBM framework does not account for such mineralogical alterations induced by chemical weathering. Second, the geometry of grains in GBMs is typically generated through Voronoi tessellation or similar schemes, resulting in idealized polyhedral particles that do not fully capture the irregular morphology, crystallographic features, and inclusions present in natural minerals. With the aid of high-resolution computed tomography (CT), it is now possible to capture the actual 3D geometry of mineral grains, as well as discontinuities such as voids and dissolution features that develop during weathering (Zhou et al. 2025). By integrating such CT-derived data with the 3D-GBM approach incorporating pre-existing microcracks, a more accurate and realistic model of weathered selenite can be constructed. Additionally, in recent years, a newer bond model has been implemented in PFC based on the work of Rasmussen (2022), namely the spring network model and the sub-spring network model. This approach has been shown to provide a more accurate representation of rock failure processes compared to previous contact models (Rasmussen and Min 2024; Potyondy et al. 2025). In future studies, applying these new bond models to investigate the microcracking behavior and AE characteristics of weathered selenite will be essential. Finally, the calibration

of microparameters in the flat-joint model suffers from non-uniqueness, as different parameter sets can reproduce similar macroscopic responses while producing markedly different microcracking patterns. This limitation raises concerns about the robustness and physical fidelity of the simulated failure processes. Therefore, future research should focus on developing more rigorous calibration strategies that minimize non-uniqueness and establish a more reliable linkage between microparameters and macroscopic rock behavior. Improvements addressing these limitations will provide new approaches for investigating the deformation behavior and AE characteristics of rocks with varying degrees of weathering. Ultimately, it will offer valuable insights and technical support for developing more effective conservation strategies for stone cultural relics affected by long-term weathering.

5 Conclusions

This work investigates the influence of weathering degree on the mechanical response, nonlinear deformation behavior, and AE characteristics of weathered selenite samples subjected to mode I loading. To accurately represent pre-existing microcracks in weathered selenite, a flat-joint model incorporating unbonded contacts was employed. Additionally, a 3D-GBM using 3D Voronoi tessellation was applied to simulate the heterogeneous crystalline microstructure of selenite. Slightly weathered selenite samples collected from the Garisenda Tower in the Bologna region were used to calibrate the microparameters of the 3D-GBM. Based on this calibration, numerical models for moderately and highly weathered selenite were developed by increasing the number and width of pre-existing microcracks. The main findings are summarized as follows:

(1) The extended 3D-GBM coupled with the flat-joint model successfully captures the nonlinear deformation behavior of weathered selenite, including both strain-softening and strain-hardening stages. With increasing weathering degree, the initial nonlinear compaction stage in the load–displacement curve becomes more pronounced, accompanied by an increase in failure displacement. Meanwhile, the mode I fracture toughness of weathered selenite decreases significantly, from 0.181 $MPa{\cdot}m^{1/2}$ in the SWS sample to 0.052 $MPa{\cdot}m^{1/2}$ in the HWS sample.

(2) The spatial distribution of force chains undergoes significant changes with increasing weathering. It becomes increasingly heterogeneous, with a small number of contacts bearing most of the applied load in HWS samples. This leads to more dispersed nucleation of microcracks. Such heterogeneous force chain distribution facilitates the propagation and coalescence of microcracks, as they tend to initiate in zones of high stress concentration.

(3) Under mode I loading, selenite samples at different weathering stages exhibit distinct AE characteristics. As weathering intensifies, AE event localization shifts from being concentrated on a single plane to a more random distribution across a larger region. Concurrently, the maximum AE magnitude decreases while the *b*-value increases, rising from 2.01 in slightly weathered samples to 3.22 in highly weathered ones. These trends indicate a transition in failure mode from brittle failure dominated by a single fracture surface to ductile failure involving multiple secondary fractures. A sudden drop in the *b*-value serves as a precursor to catastrophic failure in weathered selenite.

(4) For stone cultural heritage exposed to natural environments, a zoning-based monitoring strategy informed by weathering degree, combined with AE monitoring, can enhance the development of refined structural health assessment models. This approach offers valuable new insights for evaluating the long-term stability of stone-built heritage structures.

Overall, this work provides important insights into the effects of weathering-induced microstructural changes on the mechanical behavior, microcracking evolution, force chain distribution, and AE characteristics of selenite rocks. The numerical findings highlight the critical role of accurately modeling pre-existing microcracks and the heterogeneous crystalline microstructure in capturing the complex nonlinear deformation and failure mechanisms of weathered rocks. Furthermore, the combined use of advanced micromechanical modeling and AE monitoring demonstrates significant potential for improving the structural health assessment and preservation strategies of stone cultural heritage exposed to natural weathering processes.

Acknowledgements The authors gratefully acknowledge the financial support for this work provided by the Politecnico di Torino through its basic research funds. The first author also wishes to express his sincere gratitude to the China Scholarship Council (CSC) for the scholarship that enabled his research period at the Politecnico di Torino. Finally, the authors extend their thanks to the Municipality of Bologna for granting permission to publish this work.

Author contributions Xunjian Hu Writing – original draft, Visualization, Software, Resources, Methodology, Investigation, Formal analysis, Conceptualization; Giuseppe Lacidogna Writing – review & editing , Supervision, Funding acquisition; Pedro Marin Montanari Formal analysis, Writing – review & editing; Ediblu Silva Cezar Formal analysis, Writing – review & editing; Jueliang Chen Writing – review & editing; Angelo Di Tommaso Writing – review & editing.

Funding Open access funding provided by Politecnico di Torino within the CRUI-CARE Agreement. No funding was received for conducting this study.

Declarations

Conflict of interest The authors declare that they have no known competing financial interests or personal relationships that could have appeared to influence the work reported in this paper.

Data availability All data generated or analyzed during this work are included in this published paper and is available from the corresponding author on reasonable request.

References

Alneasan M, Behnia M (2021) An experimental investigation on tensile fracturing of brittle rocks by considering the effect of grain size and mineralogical composition. Int J Rock Mech Min Sci 137:104570. https://doi.org/10.1016/j.ijrmms.2020.104570

Baraccani S, Palermo M, Gasparini G, Trombetti T (2021) A time domain approach for data interpretation from long-term static monitoring of historical structures. Struct Control Health Monit 28(5):e2708. https://doi.org/10.1002/stc.2708

Bertolini I, Marchi M, Gottardi G (2023) Learning from a well-documented geotechnical cold case: the Two Towers of Bologna. Italy Int J Archit Herit 17(10):1607–1629. https://doi.org/10.1080/15583058.2022.2057828

Bu M, Guo P, Li X, Zhang P, Wang J (2025) Thermo-mechanical behavior of granite rocks based on the analysis of 3D grain-based numerical models. Rock Mech Rock Eng. https://doi.org/10.1007/s00603-025-04479-8

Carroll D (2012) Rock weathering. Springer, Germany

Caselle C, Bonetto S, Colombero C, Comina C (2019a) Mechanical properties of microcrystalline branching selenite gypsum samples and influence of constituting factors. J Rock Mech Geotech Eng 11(2):228–241. https://doi.org/10.1016/j.jrmge.2018.09.003

Caselle C, Bonetto S, Vagnon F, Costanzo D (2019b) Dependence of macro mechanical behaviour of gypsum on micro-scale grain-size distribution. Geotech Lett 9(4):290–298. https://doi.org/10.1680/jgele.18.00206

Dallavalle G, Di Tommaso A, Gottardi G, Trombetti T, Lancellotta R, Lugli S (2022). The Garisenda Tower in Bologna: Effects of degradation of selenite basement on its static behaviour. In Geotechnical Engineering for the Preservation of Monuments and Historic Sites III (pp. 1088–1100). CRC Press. https://doi.org/10.1201/9781003308867-86

Dehghani B, Faramarzi L (2019) Experimental investigations of fracture toughness and crack initiation in marble under different freezing and thermal cyclic loading. Constr Build Mater 220:340–352. https://doi.org/10.1016/j.conbuildmat.2019.05.196

Eppes MC, Keanini R (2017) Mechanical weathering and rock erosion by climate-dependent subcritical cracking. Rev Geophys 55(2):470–508. https://doi.org/10.1002/2017RG000557

Feignier B, Young RP (1992) Moment tensor inversion of induced microseisnmic events: Evidence of non-shear failures in the $-4 < M < -2$ moment magnitude range. Geophys Res Lett 19(14):1503–1506. https://doi.org/10.1029/92GL01130

Fort R, de Buergo MA, Perez-Monserrat EM (2013) Non-destructive testing for the assessment of granite decay in heritage structures compared to quarry stone. Int J Rock Mech Min Sci 61:296–305. https://doi.org/10.1016/j.ijrmms.2012.12.048

Ge Z, Sun Q (2018) Acoustic emission (AE) characteristics of granite after heating and cooling cycles. Eng Fract Mech 200:418–429. https://doi.org/10.1016/j.engfracmech.2018.08.011

Ghazvinian E, Diederichs MS, Quey R (2014) 3D random Voronoi grain-based models for simulation of brittle rock damage and fabric-guided micro-fracturing. J Rock Mech Geotech Eng 6(6):506–521. https://doi.org/10.1016/j.jrmge.2014.09.001

Goebel W, Schorlemmer TH, Becker D, Dresenm TW, Sammis CG (2013) Acoustic emissions document stress changes over many seismic cycles in stick-slip experiments. Geophys Res Lett 40(10):2049–2054. https://doi.org/10.1002/grl.50507

Gong H, Wang M, Luo Y, Liu T, Fan R, Li X (2025) Stress-confinement effect on the dynamic mechanical properties of heterogeneous granite under impact loading: experimental and numerical simulation. Int J Numer Anal Methods Geomech. https://doi.org/10.1002/nag.3896

Guo TY, Zhao Q (2022) Acoustic emission characteristics during the microcracking processes of granite, marble and sandstone under mode I loading. Rock Mech Rock Eng 55(9):5467–5489. https://doi.org/10.1007/s00603-022-02937-1

Gupta AS, Rao KS (2000) Weathering effects on the strength and deformational behaviour of crystalline rocks under uniaxial compression state. Eng Geol 56(3–4):257–274. https://doi.org/10.1016/S0013-7952(99)00090-3

Gutenberg B, Richter CF (1944) Frequency of earthquakes in California. Bull Seismol Soc Am 34(4):185–188

Hazzard JF, Young RP (2000) Simulating acoustic emissions in bonded-particle models of rock. Int J Rock Mech Min Sci 37(5):867–872. https://doi.org/10.1016/S1365-1609(00)00017-4

Hazzard JF, Young RP (2004) Dynamic modelling of induced seismicity. Int J Rock Mech Min Sci 41(8):1365–1376. https://doi.org/10.1016/j.ijrmms.2004.09.005

Hoek E, Martin CD (2014) Fracture initiation and propagation in intact rock–a review. J Rock Mech Geotech Eng 6(4):287–300. https://doi.org/10.1016/j.jrmge.2014.06.001

Hu X, Xie N, Zhu Q, Chen L, Li P (2020) Modeling damage evolution in heterogeneous granite using digital image-based grain-based model. Rock Mech Rock Eng 53(11):4925–4945. https://doi.org/10.1007/s00603-020-02191-3

Hu X, Gong X, Hu H, Guo P, Ma J (2022) Cracking behavior and acoustic emission characteristics of heterogeneous granite with double pre-existing filled flaws and a circular hole under uniaxial compression: insights from grain-based discrete element method modeling. Bull Eng Geol Environ 81(4):162. https://doi.org/10.1007/s10064-022-02665-4

Hu X, Shentu J, Xie N, Huang Y, Lei G, Hu H, Gong X (2023a) Predicting triaxial compressive strength of high-temperature treated rock using machine learning techniques. J Rock Mech Geotech Eng 15(8):2072–2082. https://doi.org/10.1016/j.jrmge.2022.10.014

Hu X, Liao D, Ma D, Xie S, Xie N, Hu H, Gong X (2023b) Machine learning models for predicting rock fracture toughness at different temperature conditions. Case Stud Constr Mater 19:e02622. https://doi.org/10.1016/j.cscm.2023.e02622

Hu X, Guo P, Xie N, Hu H, Lei G, Ma J, Gong X (2023c) Creep behavior and associated acoustic characteristics of heterogeneous granite containing a single pre-existing flaw using a grain-based

parallel-bonded stress corrosion model. Rock Mech Rock Eng 56(7):4799–4832. https://doi.org/10.1007/s00603-023-03291-6

Hu X, Liao D, Hu H, Xie S, Xie N, Gong X (2024a) The influence of mechanical heterogeneity of grain boundary on mechanical and microcracking behavior of granite under mode I loading using a grain-based model. Rock Mech Rock Eng 57(5):3139–3169. https://doi.org/10.1007/s00603-023-03752-y

Hu X, Lacidogna G, Xie N, Montanari PM, Gong X (2024b) Tensile microcracking behavior of granites after high temperature treatment by considering the effect of grain size and mineralogical composition. Rock Mech Rock Eng 57(12):10583–10609. https://doi.org/10.1007/s00603-024-04108-w

Huang X, Qi S, Zheng B, Liang N, Li L, Xue L, Tai D (2021) An advanced grain-based model to characterize mechanical behaviors of crystalline rocks with different weathering degrees. Eng Geol 280:105951. https://doi.org/10.1016/j.enggeo.2020.105951

Hudson JA, Pearce RG, Rogers RM (1989) Source type plot for inversion of the moment tensor. J Geophys Res Solid Earth 94(B1):765–774. https://doi.org/10.1029/JB094iB01p00765

Itasca Consulting Group Inc (2014) Particle flow code (PFC), Version 5.0. Minneapolis

Jaques DS, Marques EAG, Marcellino LC, Leão MF, Ferreira EPS, dos Santos Lemos CC (2020) Changes in the physical, mineralogical and geomechanical properties of a granitic rock from weathering zones in a tropical climate. Rock Mech Rock Eng 53:5345–5370. https://doi.org/10.1007/s00603-020-02240-x

Ji PQ, Zhang XP, Zhang Q (2018) A new method to model the nonlinear crack closure behavior of rocks under uniaxial compression. Int J Rock Mech Min Sci 112:171–183. https://doi.org/10.1016/j.ijrmms.2018.10.015

Ke B, Zhou K, Xu C, Deng H, Li J, Bin F (2018) Dynamic mechanical property deterioration model of sandstone caused by freeze–thaw weathering. Rock Mech Rock Eng 51:2791–2804. https://doi.org/10.1007/s00603-018-1495-0

Kuruppu MD, Obara Y, Ayatollahi MR, Chong KP, Funatsu T (2014) Isrm-suggested method for determining the mode I static fracture toughness using semi-circular bend specimen. Rock Mech Rock Eng 47:267–274. https://doi.org/10.1007/s00603-013-0422-7

Labus M, Bochen J (2012) Sandstone degradation: an experimental study of accelerated weathering. Environ Earth Sci 67:2027–2042. https://doi.org/10.1007/s12665-012-1642-y

Lacidogna G, Manuello A, Niccolini G, Carpinteri A (2015) Acoustic emission monitoring of Italian historical buildings and the case study of the Athena temple in Syracuse. Archit Sci Rev 58(4):290–299. https://doi.org/10.1080/00038628.2012.720246

Lan H, Martin CD, Hu B (2010) Effect of heterogeneity of brittle rock on micromechanical extensile behavior during compression loading. J Geophys Res: Solid Earth 115(B01202):1–14. https://doi.org/10.1029/2009JB006496

Lei X, Masuda K, Nishizawa O, Jouniaux L, Liu L, Ma W, Satoh T, Kusunose K (2004) Detailed analysis of acoustic emission activity during catastrophic fracture of faults in rock. J Struct Geol 26(2):247–258. https://doi.org/10.1016/S0191-8141(03)00095-6

Li Y, Bahrani N (2021) A continuum grain-based model for intact and granulated Wombeyan marble. Comput Geotech 129:103872. https://doi.org/10.1016/j.compgeo.2020.103872

Li XF, Li X, Li HB, Zhang QB, Zhao J (2018a) Dynamic tensile behaviours of heterogeneous rocks: the grain scale fracturing characteristics on strength and fragmentation. Int J Impact Eng 118:98–118. https://doi.org/10.1016/j.ijimpeng.2018.04.006

Li K, Cheng Y, Fan X (2018b) Roles of model size and particle size distribution on macro-mechanical properties of Lac du Bonnet granite using flat-joint model. Comput Geotech 103:43–60. https://doi.org/10.1016/j.compgeo.2018.07.007

Li H, Ma H, Shi X, Zhou J, Zhang H, Daemen JJK (2020) A 3D grain-based model for simulating the micromechanical behavior of salt rock. Rock Mech Rock Eng 53:2819–2837. https://doi.org/10.1007/s00603-020-02085-4

Lim IL, Johnston IW, Choi SK (1993) Stress intensity factors for semi-circular specimens under three-point bending. Eng Fract Mech 44(3):363–382. https://doi.org/10.1016/0013-7944(93)90030-V

Lin Y, Zhou K, Li J, Ke B, Gao R (2020) Weakening laws of mechanical properties of sandstone under the effect of chemical corrosion. Rock Mech Rock Eng 53:1857–1877. https://doi.org/10.1007/s00603-019-01998-z

Lin S, Wang L, Zhang W, Wang S, Zhang K, Lei Y, Jiang S, Chen H, Zhao G, Feng X (2024) Cross-scale quantitative and qualitative study of grotto sandstone under salt weathering. Rock Mech Rock Eng. https://doi.org/10.1007/s00603-024-04130-y

Liu JB, Zhang ZJ, Li B (2019) Microscopic & macroscopic characterizations of Beijing marble as a building material for UNESCO heritage sites: new insights into physico-mechanical property estimation and weathering resistance. Constr Build Mater 225:510–525. https://doi.org/10.1016/j.conbuildmat.2019.07.094

Liu X, Han M, He W, Li X, Chen D (2020) A new *b* value estimation method in rock acoustic emission testing. J Geophys Res Solid Earth 125(12):e2020JB019658. https://doi.org/10.1029/2020JB019658

Liu S, Lan H, Chen H, Huang X, Li L, Han B (2025) Differences in the failure process of grottoes sandstone in southern and northern China determined by microstructure. npj Herit Sci 13(1):1–16. https://doi.org/10.1038/s40494-025-01781-0

Lockner D (1993) The role of acoustic emission in the study of rock fracture. Int J Rock Mech Min Sci Geomech Abstr 30(7):883–899. https://doi.org/10.1016/0148-9062(93)90041-B

Lopez-Comino JA, Cesca S, Heimann S, Grigoli F, Milkereit C, Dahm T, Zang A (2017) Characterization of hydraulic fractures growth during the Äspö Hard Rock Laboratory experiment (Sweden). Rock Mech Rock Eng 50:2985–3001. https://doi.org/10.1007/s00603-017-1285-0

Luque A, Ruiz-Agudo E, Cultrone G, Sebastián E, Siegesmund S (2011) Direct observation of microcrack development in marble caused by thermal weathering. Environ Earth Sci 62:1375–1386. https://doi.org/10.1007/s12665-010-0624-1

Ma J, Wu S, Zhang XP, Gan Y (2020) Modeling acoustic emission in the Brazilian test using moment tensor inversion. Comput Geotech 123:103567. https://doi.org/10.1016/j.compgeo.2020.103567

Ma W, Wang J, Li X, Wang T (2021) Crack evolution and acoustic emission characteristics of rock specimens containing random joints under uniaxial compression. Acta Geophys 69(6):2427–2441. https://doi.org/10.1007/s11600-021-00686-3

Mahabadi OK, Tatone BSA, Grasselli G (2014) Influence of microscale heterogeneity and microstructure on the tensile behavior of crystalline rocks. J Geophys Res Solid Earth 119(7):5324–5341. https://doi.org/10.1002/2014JB011064

Mammoliti E, Cupido M, Teloni R, Tittarelli F, Giuli G, Paris E, Santini S (2024) Implementation of a non-destructive method to assess weathering deterioration of sandstones in cultural heritage. Bull Eng Geol Environ 83(4):110. https://doi.org/10.1007/s10064-024-03601-4

Marin Montanari P, Lacidogna G, Invernizzi S, Di Tommaso A, Carpinteri A (2024). Experimental and numerical damage assessment of the Garisenda Tower: Investigation by AE, thermal, seismic, and permanent strain analyses. In International Operational Modal Analysis Conference (pp. 3–14). Cham: Springer Nature Switzerland. https://doi.org/10.1007/978-3-031-61421-7_1

Mehranpour MH, Kulatilake PH (2017) Improvements for the smooth joint contact model of the particle flow code and its applications. Comput Geotech 87:163–177. https://doi.org/10.1016/j.compgeo.2017.02.012

Montes H, Duplay J, Martínez L, Escoffier S, Rousset D (2004) Structural modifications of Callovo-Oxfordian argillite under hydration/dehydration conditions. Appl Clay Sci 25:187–194. https://doi.org/10.1016/j.clay.2003.10.004

Monticelli JP, Ribeiro R, Futai M (2020) Relationship between durability index and uniaxial compressive strength of a gneissic rock at different weathering grades. Bull Eng Geol Environ 79:1381–1397. https://doi.org/10.1007/s10064-019-01625-9

Moslehy A, Alshibli KA, Truster TJ (2022) Influence of temperature and crystal orientation on compressive strength of rock salt using a newly developed high-pressure thermal cell. Rock Mech Rock Eng 55(1):91–108. https://doi.org/10.1007/s00603-021-02655-0

Mukherjee R, Misra S (2024) Insights into the micromechanics of dehydration-induced gypsum to γ-anhydrite phase transition from instrumented microindentation experiments. J Geophys Res Solid Earth 129(1):e2023JB027098. https://doi.org/10.1029/2023JB027098

Munoz-Ibanez A, Delgado-Martín J, Herbón-Penabad M, Alvarellos-Iglesias J (2021) Acoustic emission monitoring of mode I fracture toughness tests on sandstone rocks. J Pet Sci Eng 205:108906. https://doi.org/10.1016/j.petrol.2021.108906

Nicholson DT (2001) Pore properties as indicators of breakdown mechanisms in experimentally weathered limestones. Earth Surf Processes Landf: J British Geomorphol Res Group 26(8):819–838. https://doi.org/10.1002/esp.228

Niu C, Li X, Zhou L, Zhu Z, Dai F, Chen J (2024) Deterioration of dynamic fracture properties of granite under the coupled effects of hydrochemical solutions and freeze-thaw cycles. Int J Rock Mech Min Sci 177:105751. https://doi.org/10.1016/j.ijrmms.2024.105751

Okewale IA, Grobler H (2021) Inherent complexities in weathered rocks: a case of volcanic rocks. Rock Mech Rock Eng 54(11):5533–5554. https://doi.org/10.1007/s00603-021-02569-x

Peng S, Li X, Li C, Liang L, Huang L (2024) Crack-closure behavior and stress-sensitive wave velocity of hard rock based on flat-joint model in particle-flow-code (PFC) modeling. Comput Geotech 170:106320. https://doi.org/10.1016/j.compgeo.2024.106320

Pesci A, Teza G, Loddo F, Rossetti A, Gambuzzi I, Gambuzzi A (2024) The role of remote sensing to enlarge knowledge on health state of a historical building hit by earthquake: the case of Garisenda leaning tower (Bologna). Ann Geophys 67(5):S550–S550. https://doi.org/10.4401/ag-9119

Potyondy DO, Fu W, Purvance M, Mas Ivars D (2025). A 3D subspring network breakable voronoi model for rock. Rock Mechanics and Rock Engineering, 1–33. https://doi.org/10.1007/s00603-025-04655-w

Potyondy DO (2010). A grain-based model for rock: approaching the true microstructure. In: Paper presented at the proceedings of the rock mechanics in the Nordic Countries, Kongsberg, Norway, June 9–12

Potyondy DO (2012). A flat-jointed bonded-particle material for hard rock. The 46th U.S. Rock Mechanics/Geomechanics Symposium. Chicago: American Rock Mechanics Association. 12–501

Ramon A, Caselle C, Bonetto SMR, Costanzo D, Alonso EE (2021) Effect of microstructure and relative humidity on strength and creep of gypsum. Rock Mech Rock Eng 54(8):4121–4145. https://doi.org/10.1007/s00603-021-02510-2

Rasmussen LL (2022) A breakable grain-based model for bi-modular rocks. Int J Rock Mech Min Sci 151:105028. https://doi.org/10.1016/j.ijrmms.2021.105028

Rasmussen LL, Min KB (2024) Exploring heterogeneity consideration in bonded block analyses of laboratory and in situ tests on opalinus clay. Rock Mech Rock Eng 57(9):6811–6835. https://doi.org/10.1007/s00603-024-03876-9

Raziperchikolaee S, Alvarado V, Yin S (2021) Quantitative acoustic emissions source mechanisms analysis of soft and competent rocks through micromechanics-seismicity coupled modeling. Int J Geomech 21(3):04020269. https://doi.org/10.1061/(ASCE)GM.1943-5622.0001933

Saadat M, Taheri A, Kawamura Y (2021) Investigating asperity damage of natural rock joints in polycrystalline rocks under confining pressure using grain-based model. Comput Geotech 135:104144. https://doi.org/10.1016/j.compgeo.2021.104144

Sarfarazi V, Torabi-Kaveh M, Far AM (2024) Effects of weathering depth and thickness on rock failure: experimental approach and particle flow code simulation. J Rock Mech Geotech Eng 16(11):4638–4653. https://doi.org/10.1016/j.jrmge.2023.11.046

Sun W, Wu S, Guo W (2023) Study on the semi-circular bend method for characterizing the mixed mode I/II fracture toughness of sandstone: a micro-perspective. Theor Appl Fract Mech 127:104064. https://doi.org/10.1016/j.tafmec.2023.104064

Sun B, Shi W, Liang Y, Zhang H, Peng N, Yang S, Liu P (2025a) Research on the variations in the weathering of large open-air stone relics from macro-and microperspectives: a case study of the Leshan Giant Buddha. NPJ Herit Sci 13(1):102. https://doi.org/10.1038/s40494-025-01566-5

Sun B, Yan Y, Wang S, Qi C, Yang H, Zeng S (2025b) Self-organized criticality and *b*-value characteristics of acoustic emission of rocks under different stress paths. Rock Mech Rock Eng 58(1):851–866. https://doi.org/10.1007/s00603-024-04191-z

Teng M, Bi J, Zhao Y, Wang C (2023) Experimental study on shear failure modes and acoustic emission characteristics of rock-like materials containing embedded 3D flaw. Theor Appl Fract Mech 124:103750. https://doi.org/10.1016/j.tafmec.2023.103750

Tuğrul A (2004) The effect of weathering on pore geometry and compressive strength of selected rock types from Turkey. Eng Geol 75(3–4):215–227. https://doi.org/10.1016/j.enggeo.2004.05.008

Ullah B, Zhou Z, Cai X, Lu J, Zhao CC (2023) Failure prediction and microcracks development based on acoustic emission and energy evolution for different rocks treated with freeze–thaw weathering. Bull Eng Geol Environ 82(12):471. https://doi.org/10.1007/s10064-023-03485-w

Vavryčuk V (2015) Moment tensor decompositions revisited. J Seismol 19:231–252. https://doi.org/10.1007/s10950-014-9463-y

Vivoda Prodan M, Mileusnić M, Mihalić Arbanas S, Arbanas Ž (2017) Influence of weathering processes on the shear strength of siltstones from a flysch rock mass along the northern Adriatic coast of Croatia. Bull Eng Geol Environ 76:695–711. https://doi.org/10.1007/s10064-016-0881-7

Wang S, Zhou J, Zhang L, Han Z, Zhang F (2021) Parameter studies on the mineral boundary strength influencing the fracturing of the crystalline rock based on a novel grain-based model. Eng Fract Mech 241:107388. https://doi.org/10.1016/j.engfracmech.2020.107388

Wang M, Li D, Ma J, Tao J, Zhao J (2024a) Effects of fluid salinity and composition on subcritical crack growth in marble. Constr Build Mater 445:137904. https://doi.org/10.1016/j.conbuildmat.2024.137904

Wang X, Liu X, Wang E, Liu S, Shan T, Labuz JF (2024b) Microcracking characterization in tensile failure of hard coal: an experimental and numerical approach. Rock Mech Rock Eng 57(8):6441–6460. https://doi.org/10.1007/s00603-024-03827-4

Wang S, Elsworth D, Zhang L, Zhao X, Wang T (2025) Hydro-grain-texture modeling of systematics of propagation, branching, and coalescence of fluid-driven fractures. Rock Mech Rock Eng 58(1):623–644. https://doi.org/10.1007/s00603-024-04165-1

Waragai T (2016) The effect of rock strength on weathering rates of sandstone used for Angkor temples in Cambodia. Eng Geol 207:24–35. https://doi.org/10.1016/j.enggeo.2016.04.006

Wei MD, Dai F, Xu NW, Liu Y, Zhao T (2017) Fracture prediction of rocks under mode I and mode II loading using the generalized maximum tangential strain criterion. Eng Fract Mech 186:21–38. https://doi.org/10.1016/j.engfracmech.2017.09.026

Weng L, Wu Z, Wang Z, Chu Z, Xu X, Liu Q (2023) Acoustic emission source localization in heterogeneous rocks with random inclusions using a PRM-based wave velocity model. Rock Mech Rock Eng 56(5):3301–3315. https://doi.org/10.1007/s00603-023-03236-z

Wong LNY, Guo TY, Lam WK, Ng JYH (2019) Experimental study of cracking characteristics of Kowloon granite based on three mode I fracture toughness methods. Rock Mech Rock Eng 52:4217–4235. https://doi.org/10.1007/s00603-019-01882-w

Yahaghi J, Liu H, Chan A, Fukuda D (2023) Development of a three-dimensional grain-based combined finite-discrete element method to model the failure process of fine-grained sandstones. Comput Geotech 153:105065. https://doi.org/10.1016/j.compgeo.2022.105065

Yang X, Jiang XW, Ouyang KG, Ji TT, Gao YF, Geng XH, Wan L (2025) The mechanisms of salt weathering responsible for sandstone deterioration in the Yungang Grottoes, China. Eng Geol 350:107989. https://doi.org/10.1016/j.enggeo.2025.107989

Ye Y, Zeng Y, Cheng S, Chen X, Sun H (2022) Three-dimensional DEM simulation of the nonlinear crack closure behaviour of rocks. Int J Numer Anal Methods Geomech 46(10):1956–1971. https://doi.org/10.1002/nag.3376

Ye T, Chen Z, Zhang C, Li C, Wei W, Dong J (2025) A novel XRF and machine learning-based method for predicting weathered rock strength. Int J Rock Mech Min Sci 191:106130. https://doi.org/10.1016/j.ijrmms.2025.106130

Yu L, Zhang T, Wu D, Wu B, Ma L, Wei J (2022) Numerical investigation of the effect of grain size-to-particle size ratio on the dynamic fracture toughness of granite by using PFC3D-GBM. Geomech Geophys Geo-Energy Geo-Resour 8(2):72. https://doi.org/10.1007/s40948-022-00387-1

Yu X, Zuo J, Mao L, Xu X, Lei B, Zhao S (2024) Uncovering the progressive failure process of primary coal-rock mass specimens: Insights from energy evolution, acoustic emission crack patterns, and visual characterization. Int J Rock Mech Min Sci 178:105773. https://doi.org/10.1016/j.ijrmms.2024.105773

Zhang L, Nguyen NGH, Lambert S, Nicot F, Prunier F, Djeran-Maigre I (2017) The role of force chains in granular materials: from statics to dynamics. Eur J Environ Civil Eng 21(7–8):874–895. https://doi.org/10.1080/19648189.2016.1194332

Zhang C, Ji H, You S, Geng Q (2024) A novel grain growth algorithm for grain-based models for investigating the complex behavior of crystalline rock. Comput Geotech 169:106230. https://doi.org/10.1016/j.compgeo.2024.106230

Zhao Z, Yang J, Zhang D, Peng H (2017) Effects of wetting and cyclic wetting–drying on tensile strength of sandstone with a low clay mineral content. Rock Mech Rock Eng 50:485–491. https://doi.org/10.1007/s00603-016-1087-9

Zhao X, Elsworth D, He Y, Hu W, Wang T (2021) A grain texture model to investigate effects of grain shape and orientation on macro-mechanical behavior of crystalline rock. Int J Rock Mech Min Sci 148:104971. https://doi.org/10.1016/j.ijrmms.2021.104971

Zhou J, Lan H, Zhang L, Yang D, Song J, Wang S (2019) Novel grain-based model for simulation of brittle failure of Alxa porphyritic granite. Eng Geol 251:100–114. https://doi.org/10.1016/j.enggeo.2019.02.005

Zhou Z, Ullah B, Rui Y, Cai X, Lu J (2023) Predicting the failure of different rocks subjected to freeze-thaw weathering using critical slowing down theory on acoustic emission characteristics. Eng Geol 316:107059. https://doi.org/10.1016/j.enggeo.2023.107059

Zhou Y, Lv W, Li B, Liang Q, Wang S (2025) A realistic 3D grain-based modeling approach for reproducing the mechanical and failure behavior of brittle granites. Int J Rock Mech Min Sci 185:105981. https://doi.org/10.1016/j.ijrmms.2024.105981